Weak focusing approximation

In a cylindrically symmetric structure the sinusoidal motion is the exact solution of the first order differential equations of motion (Eqs. 4.15, 4.16, Classical Cyclotron Chapter), the coefficients $K_x = (1-n)/R_0^2$ and $K_y = n/R_0^2$ are independent of s. Adding drift spaces results in Hill's differential equation with periodic coefficient $K(s+S) = K(s)$ (Eq. 9.11), with solution a pseudo harmonic motion (Eq. 9.15). Due to the weak focusing the beam envelope is only weakly modulated (see below), thus also is $\beta_\mathrm{u}(s)$. In practice the modulation of $\beta_\mathrm{u}(s)$ does not exceed a few percent, justifying the introduction of the average value $\overline{\beta_\mathrm{u}}$ to approximate the phase advance by

$$\int_0^s \frac{ds}{\beta_\mathrm{u}(s)} \approx \frac{s}{\overline{\beta_\mathrm{u}}} = \nu_\mathrm{u}\frac{s}{R} \tag{9.19}$$

The right equality is obtained by applying this approximation to the phase advance per period, namely (Eq. 9.14)

$$\mu_\mathrm{u} = \int_{s_0}^{s_0+S} \frac{ds}{\beta_\mathrm{u}(s)} \approx \frac{S}{\overline{\beta_\mathrm{u}}}$$

and introducing the wave number of the N-period optical structure (Eq. 9.17) so that

$$\overline{\beta_\mathrm{u}} = \frac{R}{\nu_\mathrm{u}} \tag{9.20}$$

the wavelength of the betatron oscillation around the ring. With $k \ll 1$ and using Eq. 9.18,

$$\overline{\beta_x} = \frac{\rho_0(1+k/2)}{\sqrt{1-n}}, \quad \overline{\beta_y} = \frac{\rho_0(1+k/2)}{\sqrt{n}} \tag{9.21}$$

Substituting $\nu_\mathrm{u}\frac{s}{R}$ to $\int \frac{ds}{\beta_\mathrm{u}(s)}$ in Eq. 9.15 yields the approximate solution

$$\begin{cases} u(s) \approx \sqrt{\beta_\mathrm{u}(s)\varepsilon_\mathrm{u}/\pi}\, \cos\left(\nu_\mathrm{u}\frac{s}{R}+\phi\right) \\ u'(s) \approx -\sqrt{\frac{\varepsilon_\mathrm{u}/\pi}{\beta_\mathrm{u}(s)}}\, \sin\left(\nu_\mathrm{u}\frac{s}{R}+\phi\right) + \alpha_\mathrm{u}(s)\, \cos\left(\nu_\mathrm{u}\frac{s}{R}+\phi\right) \end{cases} \tag{9.22}$$

Beam envelopes

The beam envelope $\hat{u}(s)$ (with u standing for x or y) is determined by a particle on the maximum invariant $\varepsilon_\mathrm{u}/\pi$. It is given at all s by

$$\hat{u}(s) = \pm\sqrt{\beta_\mathrm{u}(s)\frac{\varepsilon_\mathrm{u}}{\pi}} \tag{9.23}$$

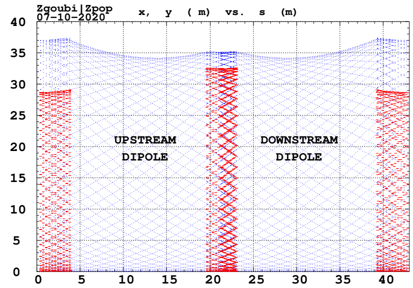

Fig. 9.12 Multi-turn particle excursion along the ZGS 2-dipole 43 m cell. The motion extrema (Eq. 9.23) tangent the envelops, respectively horizontal (red), and vertical (blue). Envelops have the symmetry of the cell

As $\beta_u(s)$ is S-periodic, so also is the envelope, $\hat{u}(s+S) = \hat{u}(s)$. In a cell with symmetries, the beam envelopes feature the same symmetries, as shown in Fig. 9.12 for the ZGS: a symmetry with respect to the center of the cell; envelope extrema are at azimuth s of $\beta_u(s)$ extrema, *i.e.* where $d\hat{u}(s)/ds \propto \beta'_u(s) = 0$ or $\alpha_u = 0$ as $\beta'_u = -2\alpha_u$.

Off-momentum orbits; *periodic dispersion*

In the linear approximation in $\Delta p/p_0$, a momentum offset $\Delta p = p - p_0$ changes mv to $mv(1+\Delta p/p_0)$ in Eq. 9.8. This changes the horizontal equation of motion (Eq. 9.10) to

$$\frac{d^2x}{ds^2} + K_x x = \frac{1}{\rho_0}\frac{\Delta p}{p_0}, \quad \text{or} \quad \frac{d^2x}{ds^2} + K_x\left(x - \frac{1}{\rho_0 K_x}\frac{\Delta p}{p_0}\right) = 0 \tag{9.24}$$

A change of variable $x - \frac{1}{K_x\rho_0}\frac{\Delta p}{p_0} \longrightarrow x$ (with $1/\rho_0 K_x = \rho_0/(1-n)$) restores the unperturbed equation of motion; thus orbits of different momenta $p = p_0 + \Delta p$ are separated by

$$\Delta x = \frac{\rho_0}{1-n}\frac{\Delta p}{p_0} \tag{9.25}$$

from the reference orbit (Fig. 9.8). Introducing the geometrical radius $R = (1+k)\rho_0$ (Eq. 9.6) to account for the added drifts, this yields the dispersion function

$$D_x = \frac{\Delta x}{\Delta p/p_0} \equiv \frac{\Delta R}{\Delta p/p_0} = \frac{R}{(1-n)(1+k)} = \frac{\rho_0}{1-n}, \quad \text{constant, positive} \tag{9.26}$$

where D_x is the chromatic dispersion of the orbits, an s-independent quantity: in a structure with axial symmetry, comprising drift sections (Fig. 9.5) or not (classical and AVF cyclotrons for instance), the ratio $\Delta x \,/\, \Delta p/p_0$ is independent of the azimuth s, so the distance of a chromatic orbit to the reference orbit is constant around the ring.

Given that $n < 1$,

- higher momentum orbits, $p > p_0$, have a greater radius,
- lower momentum orbits, $p < p_0$, have a smaller radius.

The horizontal motion of an off-momentum particle is a superposition of the betatron motion (solution of Hill's Eq. 9.22 with $\Delta p/p = 0$) and of a particular solution of the inhomogeneous equation ($\delta p/p \neq 0$), namely

$$x(s) = \sqrt{\beta_\mathrm{u}(s)\varepsilon_\mathrm{u}/\pi}\, \cos\left(\nu_\mathrm{u}\frac{s}{R} + \phi\right) + \frac{\rho_0}{1-n}\frac{\Delta p}{p_0} \tag{9.27}$$

The vertical motion is unchanged.

Chromatic orbit length

In an axially symmetric structure the difference in closed orbit length $\Delta C = 2\pi\Delta R$ resulting from the difference in momentum comes from the dipoles, as all orbits are parallel in the drifts (Fig. 9.5). Hence, from Eq. 9.26, the relative closed orbit lengthening factor, or momentum compaction, is

$$\alpha = \frac{\Delta C}{C}\Big/\frac{\Delta p}{p_0} \equiv \frac{\Delta R}{R}\Big/\frac{\Delta p}{p_0} = \frac{1}{(1-n)(1+k)} \approx \frac{1}{\nu_x^2} \tag{9.28}$$

with $k = Nl/\pi\rho_0$ (Eq. 9.6). Note that the relationship $\alpha \approx 1/\nu_x^2$ between momentum compaction and horizontal wave number established for a revolution symmetry structure (Eq. 4.21) still holds when adding drifts.

9.2.2 Acceleration

The field B in a synchrotron is varied during acceleration (a function performed by the magnet power supply) concurrently with the variation of the bunch momentum p (a function performed by the accelerating cavity) in such a way that the beam stays on the design orbit. Given the energies involved, the magnet supply imposes its law $B(t)$ (Fig. 9.13), and the cavity follows the best it can. The accelerating voltage $\hat{V}(t) = \sin\omega_\mathrm{rf}t$ is maintained in synchronism with the revolution motion by ensuring that

$$\omega_\mathrm{rf} = h\omega_\mathrm{rev} = h\frac{c}{R}\frac{B(t)}{\sqrt{\left(\frac{m_0c}{q\rho}\right)^2 + B^2(t)}}$$

Typically, for a $C = 2\pi R \approx 70$ m circumference ring[3], accelerating from $\beta = v/c \approx 0.09$ at injection (3.6 MeV protons) to $\beta \approx 1$ at top energy (3 GeV), the revolution period $T_\mathrm{rev} = C/\beta c$ and frequency $\omega_\mathrm{rev}/2\pi = 1/T_\mathrm{rev}$ span

$$\begin{cases} T_\mathrm{rev}: \ 2.6\,\mu\mathrm{s} \ \rightarrow \ 23\,\mu\mathrm{s} \\ f_\mathrm{rev}: \ 390\,\mathrm{kHz} \rightarrow 4.3\,\mathrm{MHz} \end{cases}$$

[3] Case of the SATURNE I weak focusing synchrotron (Fig. 9.1), *cf.* Exercise 9.1, Tab. 9.1

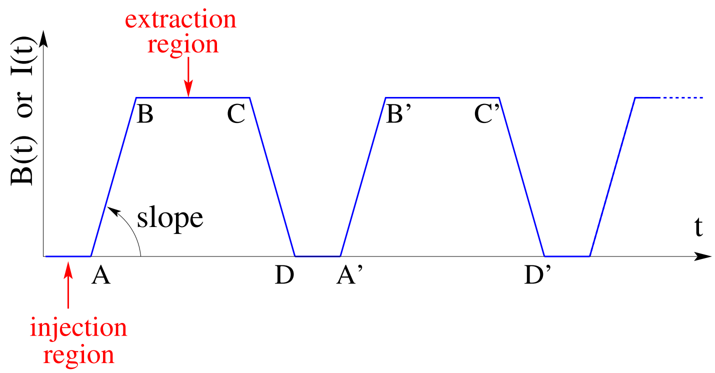

Fig. 9.13 Cycling $B(t)$ in a pulsed synchrotron. Ignoring saturation, $B(t)$ is proportional to the magnet power supply current $I(t)$. Beam injection occurs at low field, in the region of A, while extraction occurs at top energy on the high field plateau. (AB): field ramp up (acceleration); (BC): flat top; (CD): field ramp down; (DA’): thermal relaxation. (AA’): repetition period; (1/AA’): repetition rate; *slope*: ramp velocity $\dot{B} = dB/dt$ (T/s).

Energy gain

The variation of the particle energy over one turn amounts to the work of the force $F = dp/dt = q\rho dB/dt$ on the charge at the cavity, namely

$$\Delta W = F \times 2\pi R = 2\pi R q \rho \dot{B} \tag{9.29}$$

In a slow-cycling synchrotron $\dot{B}$ is usually constant over most of the acceleration cycle (Eq. 9.3), and so is ΔW. At SATURNE I, for instance

$$\frac{\Delta W}{q} = 2\pi R\rho\dot{B} = 68.9 \times 8.42 \times 1.8 = 1044\ \text{volts}$$

The field ramp lasts

$$\Delta t = (B_{\max} - B_{\min})/\dot{B} \approx B_{\max}/\dot{B} = 0.8\ \text{s}$$

The number of turns to the top energy ($W_{\max} \approx 3\,\text{GeV}$) is

$$N = \frac{W_{\max}}{\Delta W} = \frac{3\ 10^9\ \text{eV}}{1044\ \text{eV/turn}} \approx 3\ 10^6\text{turns}$$

The dependence of particle mass on field is written

$$m(t) = \gamma(t) m_0 = \frac{q\rho}{c}\sqrt{\left(\frac{m_0 c}{q\rho}\right)^2 + B(t)^2}$$

Adiabatic damping of the betatron oscillations

Particle momentum increases at the accelerating gap, resulting in a decrease of the amplitude of betatron oscillations (or, an increase if the cavity decelerates). The mechanism is sketched in Fig. 9.14 (with u standing for x or y): the slope, before and after (index 2) the cavity is

$$\frac{du}{ds} = \frac{m\frac{du}{dt}}{m\frac{ds}{dt}} = \frac{p_\mathrm{u}}{p_\mathrm{s}}, \qquad \left.\frac{du}{ds}\right|_2 = \left.\frac{m\frac{du}{dt}}{m\frac{ds}{dt}}\right|_2 = \frac{p_\mathrm{u,2}}{p_\mathrm{s,2}}$$

As the kick in momentum is longitudinal, $dp_\mathrm{u}/dt = 0$ thus $p_\mathrm{u,2} = p_\mathrm{u}$ and the increase

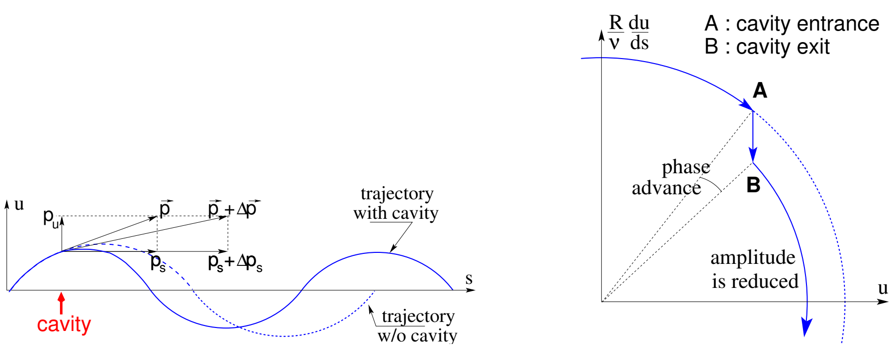

Fig. 9.14 Adiabatic damping of betatron oscillations from $u' = p_\mathrm{u}/p_\mathrm{s}$ to $u'_2 = p_\mathrm{u}/(p_\mathrm{s} + \Delta p_\mathrm{s})$ at the accelerating cavity. In transverse phase space the particle motion invariant ε_u decreases, as a result of $\Delta\left(\frac{du}{ds}\right)$

in momentum is purely longitudinal, $p_\mathrm{s,2} = p_\mathrm{s} + \Delta p_s$. Thus

$$\left.\frac{du}{ds}\right|_2 = \frac{p_\mathrm{u}}{p_\mathrm{s} + \Delta p_s} \approx \frac{p_\mathrm{u}}{p_\mathrm{s}}(1 - \frac{\Delta p_s}{p_\mathrm{s}})$$

and as a consequence the slope du/ds varies across the cavity,

$$\Delta\left(\frac{du}{ds}\right) = \left.\frac{du}{ds}\right|_2 - \frac{du}{ds} = -\frac{du}{ds}\frac{\Delta p_\mathrm{s}}{p_\mathrm{s}}$$

The variation of the slope is proportional to the slope. If $\Delta p/p > 0$ (acceleration) then the slope decreases. This variation has two consequences on the betatron oscillation (Fig. 9.14):

- a change of the betatron phase,
- a modification of the betatron amplitude.

Coordinate transport

At the cavity

$$\begin{cases} u_2 = u \\ u_2' \approx \frac{p_u}{p_s}(1 - \frac{dp}{p}) = u'(1 - \frac{dp}{p}) \end{cases}$$

In matrix form,

$$\begin{pmatrix} u_2 \\ u_2' \end{pmatrix} = [C] \begin{pmatrix} u \\ u' \end{pmatrix} \quad \text{with} \quad [C] = \begin{bmatrix} 1 & 0 \\ 0 & 1 - \frac{dp}{p} \end{bmatrix} \tag{9.30}$$

Since $det[C] = 1 - \frac{dp}{p} \neq 1$ the system is non-conservative and the area of the beam ellipse in phase space is not conserved. Assume one cavity in the ring and note $[T] \times [C]$ the one-turn coordinate transport matrix with origin at entrance of the cavity. Its determinant is

$$det[T] \times det[C] = det[C] = 1 - \frac{dp}{p}$$

The variation of the transverse ellipse area satisfies $\varepsilon_u = (1 - \frac{dp}{p_0})\varepsilon_0$ or, with $d\varepsilon_u = \varepsilon_u - \varepsilon_0$, $\frac{d\varepsilon_u}{\varepsilon_u} = -\frac{dp}{p_0}$, The solution is

$$p\ \varepsilon_u = \text{constant, or} \quad \beta\gamma\varepsilon_u = \text{constant} \tag{9.31}$$

Over N turns the coordinate transport matrix is $[T_N] = ([T][C])^N$, thus the ellipse areachanges by a factor

$$det[C]^N = (1 - \frac{dp}{p})^N \approx 1 - N\frac{dp}{p}$$

Phase stability

Synchrotron motion uses the mechanism of phase stability, or longitudinal focusing (Fig. 9.15), to stabilize the longitudinal motion of a particle in the vicinity of a synchronous phase, ϕ_s. It requires

(i) the presence of an RF cavity with its frequency locked to the revolution time,

(ii) the bunch centroid positioned either on the rising slope of the oscillating voltage (low energy regime), or on the falling slope (high energy regime).

The synchronous (or "ideal") particle follows the equilibrium trajectory (the reference closed orbit about which all other particles undergo betatron oscillation). Its velocity satisfies $v(t) = \frac{qB\rho(t)}{m}$; at each turn it reaches the accelerating gap when the oscillating voltage is at the synchronous phase ϕ_s, and undergoes an energy gain

$$\Delta W = q\hat{V}\sin\phi_s$$

The condition $|\sin\phi_s| < 1$ imposes a lower limit to the cavity voltage for acceleration to happen. According to Eq. 9.29,

$$\hat{V} > 2\pi R\rho\dot{B}$$

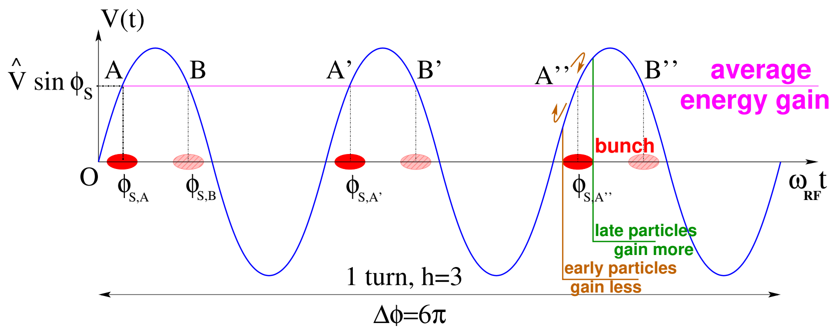

Fig. 9.15 A sketch of the mechanism of phase stability, $h = 3$ in this example. Below transition phase stability occurs for a synchronous phase taken at either one of A, A', A" arrival times at the gap. Beyond transition the stable phase is at either one of B, B', B' locations.

Referring to Fig. 9.15, the synchronous phase can be placed on the left (A, A', A" ... series) or on the right (B, B', B" ... series) of the oscillating voltage crest. One and only one of these two possibilities, and which one depending upon the optical lattice and on particle energy, ensures that particles in a bunch remain grouped in the vicinity of the synchronous particle. The transition is between two time-of-flight regimes: a particle which gains momentum compared to the synchronous particle has a greater velocity, while

- in the high bunch energy regime the increase in path length around the ring is faster than the increase in velocity (velocity essentially does not even change in ultrarelativistic regime), a revolution around the ring takes more time (this is the classical cyclotron and synchrocyclotron regime, and as well the high energy electron synchrotron regime); consider such a particle, arriving at the accelerating gap late ($\phi(t) > \phi_s$), in order for it to be pulled toward bunch center (*i.e.*, take less time around the ring) it has to undergo deceleration; this is the B series, above transition;

- in the low bunch energy regime velocity increase is faster than path length increase, thus a revolution around the ring is faster; consider such a particle, arriving at the accelerating gap early ($\phi(t) < \phi_s$), in order for it to be pulled toward bunch center (*i.e.*, take more time around the ring) it has to be slowed down, to undergo deceleration; this is the A series, below transition.

Transition energy

The transition between the two time-of-flight regimes occurs when $\dfrac{dT_{\text{rev}}}{T_{\text{rev}}} = 0$. With $T = 2\pi/\omega = C/v$, this can be written

$$\frac{d\omega_{\text{rev}}}{\omega_{\text{rev}}} = -\frac{dT_{\text{rev}}}{T_{\text{rev}}} = \frac{dv}{v} - \frac{dC}{C}$$

With $\frac{dv}{v} = \frac{1}{\gamma^2}\frac{dp}{p}$ and momentum compaction $\alpha = \dfrac{dC}{C} / \frac{dp}{p}$, (Eq. 9.28), it becomes

$$\frac{d\omega_{\text{rev}}}{\omega_{\text{rev}}} = -\frac{dT_{\text{rev}}}{T_{\text{rev}}} = \left(\frac{1}{\gamma^2} - \alpha\right)\frac{dp}{p} = \eta\frac{dp}{p} \tag{9.32}$$

which introduces the phase slip factor

$$\eta = \overbrace{\frac{1}{\gamma^2}}^{\text{kinematics}} - \underbrace{\alpha}_{\text{lattice}} = \frac{1}{\gamma^2} - \frac{1}{\gamma_{\text{tr}}^2} \tag{9.33}$$

The "transition gamma", γ_{tr}, is a property of the lattice.

In a weak focusing lattice $\gamma_{\text{tr}} = 1/\sqrt{\alpha} \approx \nu_x$ (Eq. 9.28 and Classical Cyclotron's Eq. 4.21). Thus the phase stability regime is

$$\begin{aligned} &\text{below transition, } i.e.\ \phi_s < \pi/2, \quad \text{if} \quad \gamma < \nu_x \\ &\text{above transition, } i.e. \phi_s > \pi/2, \quad \text{if} \quad \gamma > \nu_x \end{aligned} \tag{9.34}$$

In a weak focusing synchrotron the horizontal tune $\nu_x = \sqrt{(1-n)R/\rho_0}$ (Eq. 9.18) may be $\gtrless 1$, and subsequently $\gamma_{\text{tr}} > 1$ is a possibility. There is no transition gamma if $\nu_x < 1$. At SATURNE I for instance, with $\nu_x \approx 0.7$ (Tab. 9.1) and $\gamma_{\text{tr}} < 1$. So, ramping in energy did not require crossing transition-gamma[4].

9.2.3 Depolarizing Resonances

The field index is zero in the ZGS, transverse focusing is ensured by wedge angles at the ends of the eight dipoles, the only locations where non-zero horizontal field components are found. The latter are weak and as a consequence so also are depolarizing resonances: *"As we can see from the table, the transition probability* [*from spin state $\psi_{1/2}$ to spin state $\psi_{-1/2}$*] *is reasonably small up to $\gamma = 7.1$"* [12], *i.e.* proton $G\gamma = 12.73$, $p = 6.6$ GeV/c. The table referred to stipulates a transition probability

[4] Transition-gamma crossing is a common beam manipulation during acceleration in strong focusing synchrotrons. Longitudinally it requires an RF phase jump, the technique is addressed in Chapter 10.

$P_{\frac{1}{2},-\frac{1}{2}} < 0.042$, whereas resonances beyond that energy range feature $P_{\frac{1}{2},-\frac{1}{2}} > 0.36$. Beam depolarization up to 6 GeV/c, under the effect of these resonances, is illustrated in Fig. 9.16.

In a synchrotron using gradient dipoles, particles experience radial fields $B_x(y) = -n\frac{B_0}{\rho_0}y$ as they undergo vertical betatron oscillations [12, 20, 21]. As n is small these radial field components are weak, and so is their effect on spin motion.

Assuming a defect-free ring, the vertical betatron motion excites "intrinsic" spin resonances, located at

$$G\gamma_R = k\,P \pm \nu_y, \qquad k \in \mathbb{N}$$

with P the period of the ring. In the ZGS for instance, $\nu_y \approx 0.8$ (Tab. 9.2), the ring is P=4-periodic, thus $G\gamma_R = 4k \pm 0.8$. Strongest resonances are located at

$$G\gamma_R = k\,m\,P \pm \nu_y$$

with m the number of cells per superperiod [22, Sec. 3.II]. In the ZGS, with m=2 the strongest resonances occur at (Fig. 9.16)

$$G\gamma_R = 2 \times 4k \pm 0.8 = 7.2\ (3.65\,\mathrm{GeV/c});\ 8.8\ (4.51\,\mathrm{GeV/c});\ 15.2\ (7.9\,\mathrm{GeV/c});\ \ldots$$

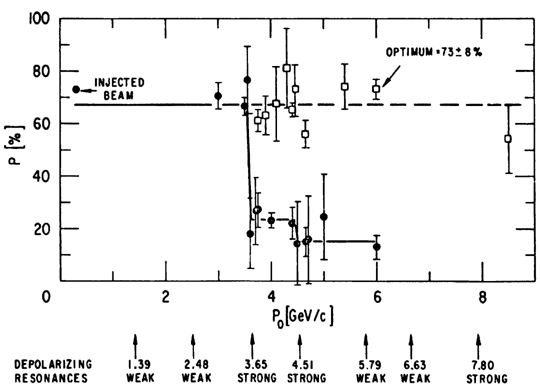

Fig. 9.16 Polarization loss at the ZGS [23] through the strong intrinsic resonances $G\gamma_R = 7.2$ ($p = 3.65\,\mathrm{GeV/c}$) and 8.8 (4.51 GeV/c) (black circles). A tune jump method preserves polarization (empty circles)

In the presence of vertical orbit defects, non-zero periodic transverse fields are experienced along the closed orbit, they excite "imperfection", *aka* "integer", depolarizing resonances, located at

$$G\gamma_R = k, \qquad k \in \mathbb{N}$$

In the case of systematic defects the periodicity of the orbit is that of the lattice, P, imperfection resonances are located at $G\gamma_R = kP$. The strongest imperfection resonances are located at [22, Sec. 3.II]

$$G\gamma_R = k\,m\,P$$

Spin precession axis. Resonance width

Consider the spin vector

$$\mathbf{S}(\theta) = (S_\eta, S_\xi, S_y)$$

of a particle, in the laboratory frame, with θ the orbital angle around the accelerator. Introduce the projection $s(\theta)$ of $\mathbf{S}$ in the median plane

$$s(\theta) = S_\eta(\theta) + jS_\xi(\theta) \qquad (\text{and } \; S_y^2 = 1 - s^2) \tag{9.35}$$

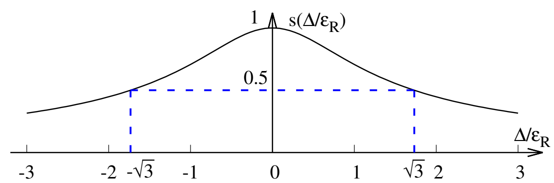

Fig. 9.17 Modulus of the horizontal projection of the spin, $s = \sqrt{1 - S_y^2}$, as a function to the distance to the resonance normalized to the resonance strength. $s = 1/2$ at distance $\Delta = \pm\sqrt{3}\epsilon_R$ from $G\gamma_R$

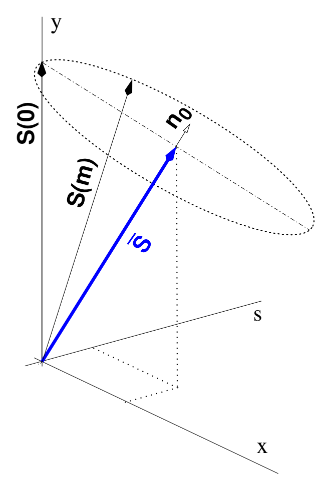

Fig. 9.18 Near an integer resonance, at any azimuth θ around the ring spins $\mathbf{S}(m)$ (m is the turn number, $\mathbf{S}(m)$ started vertical, here) precess at frequency $\omega = \sqrt{\Delta^2 + |\epsilon_R|^2}$ around a stationary axis $\mathbf{n}_0(\theta)$, whose orientation varies along the ring. $\mathbf{n}_0$ is aligned along $\overline{\mathbf{S}}$, average of $\mathbf{S}(m)$ over turns

In the case of a stationary solution of the spin motion, viz. stationary spin precession axis around the ring (Fig. 9.18) [21, Sect. 3.6.1], s satisfies [21] (Fig. 9.17)

$$s^2 = \frac{1}{1 + \frac{\Delta^2}{|\epsilon_R|^2}} \tag{9.36}$$

with $\Delta = G\gamma - G\gamma_R$ the distance to the resonance; thus the resonance width appears to be a measure of its strength. The quantity of interest is the angle, ϕ, of the spin

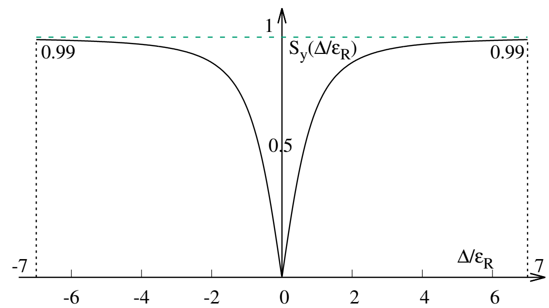

Fig. 9.19 Dependence of polarization on the distance to the resonance. For instance $S_y = 0.99$, 1% depolarization, corresponds to $\Delta = \pm 7|\epsilon_R|$. On the resonance, $\Delta = 0$, the precession axis lies in the median plane, $S_y = 0$

precession direction to the vertical axis. It is given by (Fig. 9.19)

$$\cos\phi(\Delta) \equiv S_y(\Delta) = \sqrt{1 - s^2} = \frac{\Delta/|\epsilon_R|}{\sqrt{1 + \Delta^2/|\epsilon_R|^2}} \tag{9.37}$$

On the resonance, with $\Delta = 0$, the spin precession axis lies in the bend plane: $\phi = \pm\pi/2$. A depolarization by 1% ($S_y = 0.99$) corresponds to a distance to the resonance $\Delta = 7|\epsilon_R|$, spin precession axis at an angle $\phi = \text{acos}(0.99) = 8^o$ from the vertical.

Conversely, given S_y,

$$\frac{\Delta^2}{|\epsilon_R|^2} = \frac{S_y^2}{1 - S_y^2} \tag{9.38}$$

The precession axis is common to all spins, while S_y is a measure of the polarization along the vertical axis,

$$S_y = \frac{N^+ - N^-}{N^+ + N^-}$$

where N^+ and N^- denote the number of particles in spin states $\frac{1}{2}$ and $-\frac{1}{2}$ respectively.

Things complicate a little in the vicinity of an intrinsic resonance [21, Sect. 3.6.2], the precession axis is not stationary, it precesses itself around the vertical, Fig. 9.20.

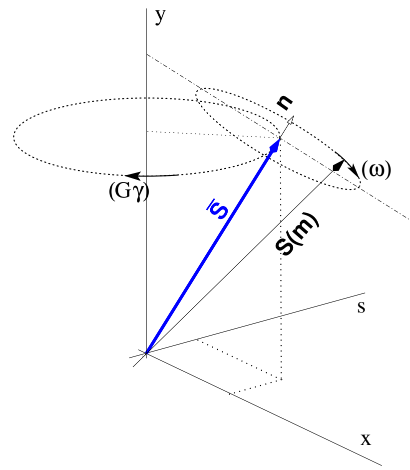

Fig. 9.20 Near an intrinsic resonance, spins $\mathbf{S}(m)$ precess at frequency ω around an axis $\mathbf{n}$, which itself precesses around the vertical axis at frequency $G\gamma$

Resonance crossing

Crossing an isolated depolarizing resonance (Figs. 9.16, 9.21) causes a loss of polarization given by the Froissart-Stora formula [24] [21, Sect. 2.3.6],

$$\frac{P_f}{P_i} = 2e^{-\frac{\pi}{2}\frac{|\epsilon_R|^2}{\alpha}} - 1 \tag{9.39}$$

from a value P_i upstream to an asymptotic value P_f downstream of the resonance. Here ϵ_R is the strength of the resonance [21, Sect. 2.3.5], and

$$\alpha = G\frac{d\gamma}{d\theta} = \frac{1}{2\pi}\frac{\Delta E}{M} \tag{9.40}$$

is the crossing speed for an energy gain ΔE per turn.

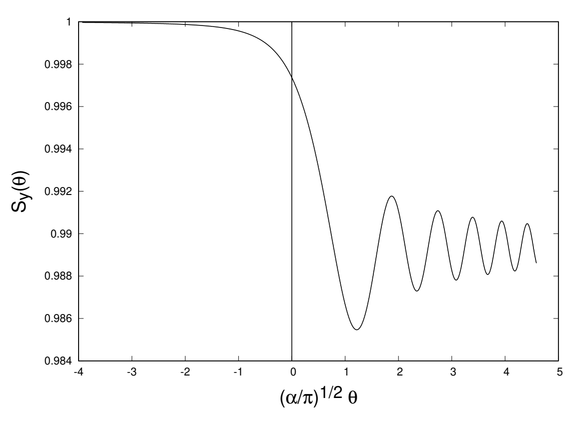

Fig. 9.21 Vertical component of spin motion $S_y(\theta)$ through a weak depolarizing resonance (Eq. 9.41). The vertical line is at the location of the resonance, which coincides with the origin of the orbital angle

Spin motion through weak resonances

Depolarizing resonances are weak up to several GeV in a weak focusing synchrotron because the radial and/or longitudinal fields are weak. Thus assume $S_{\mathrm{y,f}} \approx S_{\mathrm{y,i}}$, with $S_{\mathrm{y,f}}$ and $S_{\mathrm{y,i}}$ the asymptotic vertical spin component values respectively upstream and downstream of the resonance. With the origin of the orbital angle taken at the resonance (Fig. 9.21), and introducing the Fresnel integrals [21]

$$C(x) = \int_0^x \cos\left(\frac{\pi}{2}t^2\right)\,dt, \qquad S(x) = \int_0^x \sin\left(\frac{\pi}{2}t^2\right)\,dt$$

the polarization satisfies

$$\begin{aligned}
&\text{if } \theta < 0: \ \left(\frac{S_{\mathrm{y}}(\theta)}{S_{\mathrm{y,i}}}\right)^2 = 1 - \frac{\pi|\epsilon_R|^2}{\alpha}\left\{\left[\tfrac{1}{2} - C\left(-\theta\sqrt{\frac{\alpha}{\pi}}\right)\right]^2 + \left[\tfrac{1}{2} - S\left(-\theta\sqrt{\frac{\alpha}{\pi}}\right)\right]^2\right\}\\
&\text{if } \theta > 0: \ \left(\frac{S_{\mathrm{y}}(\theta)}{S_{\mathrm{y,i}}}\right)^2 = 1 - \frac{\pi|\epsilon_R|^2}{\alpha}\left\{\left[\tfrac{1}{2} + C\left(\theta\sqrt{\frac{\alpha}{\pi}}\right)\right]^2 + \left[\tfrac{1}{2} + S\left(\theta\sqrt{\frac{\alpha}{\pi}}\right)\right]^2\right\}
\end{aligned} \tag{9.41}$$

In the asymptotic limit,

$$\frac{S_y(\theta)}{S_{\mathrm{y,i}}} \xrightarrow{\theta\longrightarrow\infty} 1 - \frac{\pi}{\alpha}|\epsilon_R|^2 \tag{9.42}$$

which agrees with the development of Froissart-Stora formula, Eq. 9.39, to first order in $|\epsilon_R|^2/\alpha$. This approximation holds in the limit that higher order terms can be neglected: $|\epsilon_R|^2/\alpha \ll 1$.

9.3 Exercises

9.1 Construct SATURNE I (weak index) synchrotron. Spin Resonances
Solution: page 317.

In this exercise, the weak focusing 3 GeV synchrotron SATURNE I (Fig. 9.1) is modeled. Spin resonances in a weak dipole gradient lattice are observed.

Table 9.1 Parameters of SATURNE I weak focusing synchrotron [25]. ρ_0 denotes the reference bending radius in the dipole; the reference orbit, field index, wave numbers, etc., are taken along that radius

Orbit length, C	cm	6890
Average radius, $R = C/2\pi$	cm	1096.58
Drift length, $2l$	cm	400
Magnetic radius, ρ_0	cm	841.93
$R/\rho_0 = 1 + k$		1.30246
Field index n, nominal		0.6
Wave numbers ν_x, ν_y, nominal		0.72, 0.89
Stability limit		$0.5 < n < 0.757$
Injection energy (proton)	MeV	3.6
Field at injection	kG	0.326
Top energy	GeV	2.94
Field at top energy, $B_{\max}$	kG	14.9
$\dot{B}$	kG/s	18
Synchronous energy gain	keV/turn	1.160
RF harmonic		2

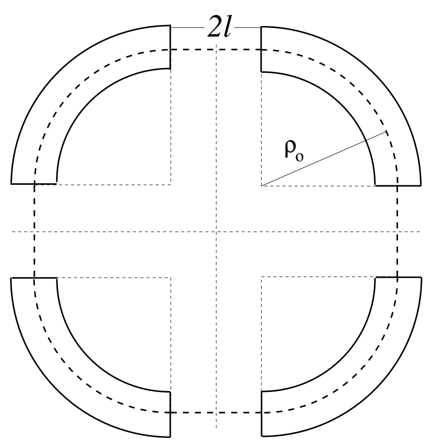

Fig. 9.22 A schematic layout of SATURNE I, a $2\pi/4$ axial symmetry structure, comprised of 4 radial field index 90 deg dipoles and 4 drift spaces. The cell in the simulation exercises is taken as a $\pi/2$ quadrant: half-drift / 90^o-dipole / half-drift

(a) Construct a model of SATURNE I 90^o cell dipole in the hard-edge model, using DIPOLE. Use the parameters given in Tab. 9.1, and Fig. 9.22 as a guidance. For beam monitoring purposes, split the dipole in two 45^odeg halves. It is judicious to take RM=841.93 cm in DIPOLE, as this is the reference radius for the definition of the radial index. Take an integration step size in centimeter range - small enough to ensure numerical convergence, as large as doable for fast multiturn raytracing.

Validate the model by producing the 6×6 transport matrix of the cell dipole (MATRIX[IFOC=0] can be used for that, with OBJET[KOBJ=5] to define a proper set of paraxial initial coordinates) and checking against theory (Sect. 15.2, Eq. 15.6).

(b) Construct a model of SATURNE I cell, with origin at the center of the drift. Find the closed orbit, that particular trajectory which has all its coordinates zero in the drifts: use DIPOLE[KPOS] to cancel the closed orbit coordinates at DIPOLE ends. While there, check the expected value of the dispersion (Eq. 9.26) and of the momentum compaction (Eq. 9.28), from the raytracing of a chromatic closed orbit - *i.e.*, the orbit of an off-momentum particle. Plot these two orbits (on- and off-momentum), over a complete turn around the ring, on a common graph.

Compute the cell periodic optical functions and tunes, using either MATRIX[IFOC=11] or TWISS; check their values against theory. Check consistency with previous dispersion function and momentum compaction outcomes.

Move the origin of the lattice at a different azimuth s along the cell: verify that, while the transport matrix depends on the origin, its trace does not.

Produce a graph of the optical functions (betatron functions and dispersion) along the cell. Check the expected average values of the betatron functions (Eq. 9.21).

Produce a scan of the tunes over the field index range $0.5 \le n \le 0.757$. REBELOTE can be used to repeatedly change n over that range. Superimpose the theoretical curves $\nu_x(n)$, $\nu_y(n)$.

(c) Justify considering the betatron oscillation as sinusoidal, namely,

$$y(\theta) = A\,\cos(\nu_y \theta + \phi)$$

wherein $\theta = s/R$, $R = \oint ds/2\pi$.

(d) Launch a few particles evenly distributed on a common paraxial horizontal Courant-Snyder invariant, vertical motion taken null (OBJET[KOBJ=8] can be used), for a single pass through the cell. Store particle data along the cell in zgoubi.plt, using DIPOLE[IL=2] and DRIFT[split,N=20,IL=2]. Use these to generate a graph of the beam envelopes.

Using Eq. 9.23 compare with the results obtained in (b). Find the minimum and maximum values of the betatron functions, and their azimuth $s(min[\beta_x])$, $s(max[\beta_x])$. Check the latter against theory.

Repeat for the vertical motion, taking $\varepsilon_x = 0$, ε_y paraxial.

Repeat, using, instead of several particles on a common invariant, a single particle traced over a few tens of turns.

(e) Produce an acceleration cycle from 3.6 MeV to 3 GeV, for a few particles launched on a common $10^{-4}\,\pi$m initial invariant in each plane. Ignore synchrotron motion (CAVITE[IOPT=3] can be used in that case). Take a peak voltage $\hat{V} = 200$ kV (unrealistic though, as it would result in a nonphysical $\dot{B}$ (Eq. 9.29)) and synchronous phase $\phi_s = 150$ deg (justify $\phi_s > \pi/2$).

Check the betatron damping over the acceleration range: compare with theory (Eq. 9.31).

How close to symplectic the numerical integration is (it is by definition *not* symplectic, being a truncated Taylor series method [26, Eq. 1.2.4]), depends on the integration step size, and on the size of the flying mesh in the DIPOLE method [26, Fig. 20]; check a possible departure of the betatron damping from theory as a function of these parameters.

Produce a graph of the horizontal and vertical wave number values over the acceleration cycle.

(f) Some spin motion, now. Adding SPNTRK at the beginning of the sequence used in (e) will ensure spin tracking.

Based on the input data file worked out for question (d), simulate the acceleration of a single particle, through the intrinsic resonance $G\gamma_R = 4 - \nu_y$, from a distance of a few times the resonance strength upstream (this requires determining BORO value under OBJET) to a distance of a few times the resonance strength downstream of the resonance, at an acceleration rate of 10 kV/turn.

OBJET[KOBJ=8] can be used to allow to easily define an initial invariant value.

Start with spin vertical. On a common graph, plot $S_y(turn)$ for a few different values of the vertical betatron invariant (the horizontal invariant value does not matter - explain that statement, it can be taken zero). Derive the resonance strength from this tracking, check against theory.

Repeat, for different crossing speeds.

Push the tracking beyond $G\gamma = 2{\times}4{+}\nu_y$: verify that the sole systematic resonances $G\gamma = \text{integer} \times P \pm \nu_y$ are excited - with $P = 4$ the periodicity of the ring.

Break the 4-periodicity of the lattice by perturbing the index in one of the 4 dipoles (say, by 10%), verify that all resonances $G\gamma = \text{integer} \pm \nu_y$ are now excited.

(g) Consider a case of weak resonance crossing, single particle (*i.e.*, a case where $P_f/P_i \approx 1$, taken from (f); crossing speed may be increased, or particle invariant decreased if needed), show that it satisfies Eq. 9.41. Match its turn-by-turn tracking data to Eq. 9.41 so to get the vertical betatron tune ν_y, the location of the resonance $G\gamma_{\mathrm{R}}$, and its strength.

(h) Stationary spin motion (*i.e.* at fixed energy) is considered in this question. Track a few particles with distances from the resonance $\Delta = G\gamma - G\gamma_R = G\gamma - (4-\nu_y)$ evenly spanning the interval $\Delta \in [0, 7 \times \epsilon_R]$.

Produce on a common graph the spin motion $S_y(turn)$ for these particles, as observed at some azimuth along the ring.

Produce a graph of $\langle S_y \rangle|_{\mathrm{turn}}(\Delta)$ (as in Fig. 9.19). Produce the vertical betatron tune ν_y, the location of the resonance $G\gamma_{\mathrm{R}}$, and its strength, obtained from a match of $\langle S_y \rangle|_{\mathrm{turn}}(\Delta)$ to (Eq. 9.37)

$$\langle S_y \rangle (\Delta) = \frac{\Delta}{\sqrt{|\epsilon_R|^2 + \Delta^2}}$$

(i) Track a 200-particle 6-D bunch, with Gaussian transverse densities of $\varepsilon_{\mathrm{x,y}}$ a few μm, and Gaussian $\delta p/p$ with $\sigma_{\delta p/p} = 10^{-4}$. Produce a graph of the average value of S_y over a 200 particle set, as a function of $G\gamma$, across the $G\gamma_R = 4 - \nu_y$ resonance. Indicate on that graph the location of the resonant $G\gamma_R$ values.

Perform this resonance crossing for five different values of the particle invariant: $\varepsilon_y/\pi = 2,\ 10,\ 20,\ 40,\ 200\,\mu$m. Compute P_f/P_i in each case, check the dependence on ε_y against theory.

Compute the resonance strength, ε_y, from this tracking.

Re-do this crossing simulation for a different crossing speed (take for instance $\hat{V} = 10\,$kV) and a couple of vertical invariant values, compute P_f/P_i so obtained. Check the crossing speed dependence of P_f/P_i against theory.

9.2 Construct the ZGS (zero-gradient) synchrotron. Spin Resonances

Solution: page 341.

In this exercise, the ZGS 12 GeV synchrotron is modeled. Spin resonances in a zero-gradient, wedge focusing synchrotron are studied.

A photo taken in the ZGS tunnel is given in Fig. 9.4; a schematic layout of the ring is shown in Fig. 9.23, and a sketch of the double dipole cell in Fig. 9.24. Table 9.2 details the parameters of the synchrotron resorted to in these simulations.

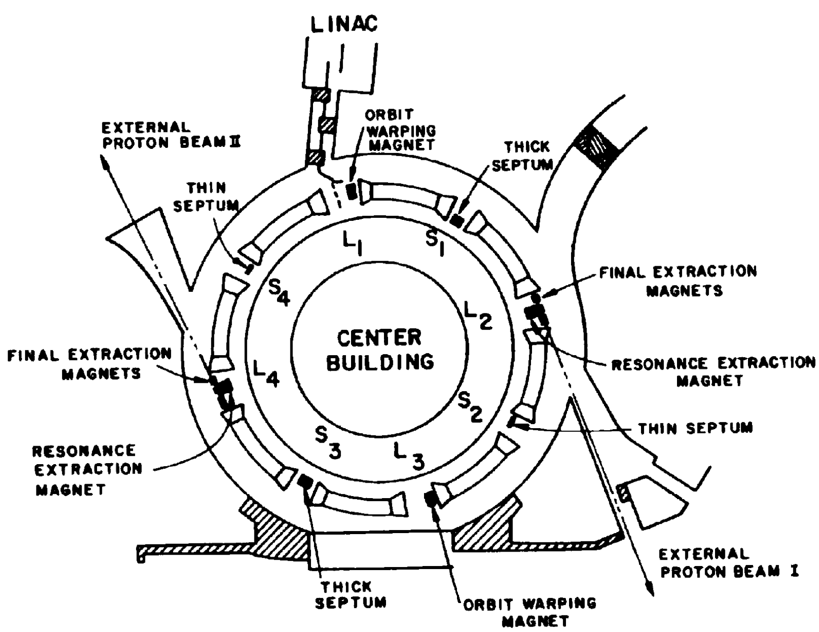

Fig. 9.23 A schematic layout of the ZGS [23], a $\pi/2$-periodic structure, comprised of 8 zero-index dipoles, 4 long and 4 short straight sections

(a) Construct a model of ZGS 45^o cell dipole in the hard-edge model, using DIPOLE. Use the parameters given in Tab. 9.2, and Figs. 9.23, 9.24 as a guidance. For beam monitoring purposes, split the dipole in two 22.5^odeg halves. Take the closed orbit radius as the reference RM=2076 cm in DIPOLE: it will be assumed that the orbit is the same at all energies[5]. Take an integration step size in centimeter range - small enough to ensure numerical convergence, as large as doable for fast multiturn raytracing.

Validate the model by producing the 6×6 transport matrices of both dipole (MATRIX[IFOC=0] can be used for that, with OBJET[KOBJ=5] to define a proper set of paraxial initial coordinates) and checking against theory (Sect. 15.2, Eq. 15.6).

Add fringe fields in DIPOLE[λ,$C_0 - C_5$], the rest if the exercise will use that model. Take fringe field extent and coefficient values

$$\lambda = 60\,\mathrm{cm}\ C_0 = 0.1455,\ C_1 = 2.2670,\ C_2 = -0.6395,\ C_3 = 1.1558,\ C_4 = C_5 = 0 \tag{9.43}$$

($C_0 - C_5$ determine the shape of the field fall-off, they have been computed from a typical measured field profile $B(s)$).

(b) Construct a model of ZGS cell accounting for dipole fringe fields, with origin at the center of the long drift. In doing so, use DIPOLE[KPOS] to cancel the closed orbit coordinates at DIPOLE ends.

Compute the periodic optical functions at cell ends, and cell tunes, using MATRIX[IFOC=11]; check their values against theory.

Move the origin at the location (azimuth s along the cell) of the betatron functions extrema: verify that, while the transport matrix depends on the origin, its trace does not. Verify that the local betatron function extrema, and the dispersion function, have the expected values.

Produce a graph of the optical functions (betatron functions and dispersion) along the cell.

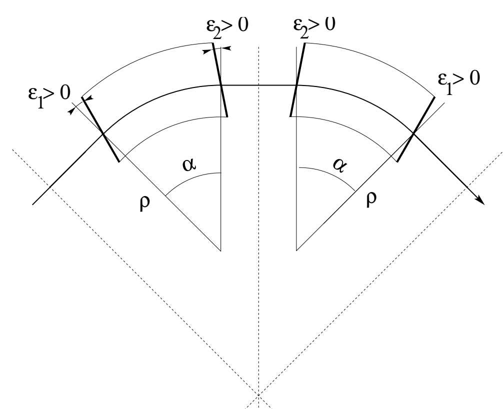

Fig. 9.24 A sketch of ZGS cell layout. In defining the entrance and exit faces (EFBs) of the magnet, beam goes from left to right. Wedge angles at the long straight sections (ε_1) and at the short straight sections (ε_2) are different

(c) Additional verifications regarding the model.

Produce a graph of the field B(s)

[5] Note that in reality the reference orbit in ZGS moved outward during acceleration [27].

Table 9.2 Parameters of the ZGS weak focusing synchrotron after Refs. [27, 28] [23, pp. 288-294,p. 716] (2nd column, when they are known) and in the present simplified model and numerical simulations (3rd column). Note that the actual orbit moves during ZGS acceleration cycle, tunes change as well - this is not taken into account in the present modeling, for simplicity

<table>
<tr><th></th><th></th><th>From Refs. [27, 28]</th><th>Simplified model</th></tr>
<tr><td>Injection energy</td><td>MeV</td><td colspan="2">50</td></tr>
<tr><td>Top energy</td><td>GeV</td><td colspan="2">12.5</td></tr>
<tr><td>$G\gamma$ span</td><td></td><td colspan="2">1.888387 - 25.67781</td></tr>
<tr><td>Length of central orbit</td><td>m</td><td>171.8</td><td>170.90457</td></tr>
<tr><td>Length of straight sections, total</td><td>m</td><td>41.45</td><td>40.44</td></tr>
<tr><td>Lattice</td><td></td><td></td><td></td></tr>
<tr><td>Wave numbers ν_x; ν_y</td><td></td><td>0.82; 0.79</td><td>0.849; 0.771</td></tr>
<tr><td>Max. β_x; β_y</td><td>m</td><td></td><td>32.5; 37.1</td></tr>
<tr><td>Magnet</td><td></td><td></td><td></td></tr>
<tr><td>Length</td><td>m</td><td>16.3</td><td>16.30486 (magnetic)</td></tr>
<tr><td>Magnetic radius</td><td>m</td><td>21.716</td><td>20.76</td></tr>
<tr><td>Field min.; max.</td><td>kG</td><td>0.482; 21.5</td><td>0.4986; 21.54</td></tr>
<tr><td>Field index</td><td></td><td colspan="2">0</td></tr>
<tr><td>Yoke angular extent</td><td>deg</td><td>43.02590</td><td>45</td></tr>
<tr><td>Wedge angle</td><td>deg</td><td>$\approx$10</td><td>13 and 8</td></tr>
<tr><td>RF</td><td></td><td></td><td></td></tr>
<tr><td>Rev. frequency</td><td>MHz</td><td>0.55 - 1.75</td><td>0.551 - 1.751</td></tr>
<tr><td>RF harmonic h=$\omega_{\mathrm{rf}}/\omega_{\mathrm{rev}}$</td><td></td><td colspan="2">8</td></tr>
<tr><td>Peak voltage</td><td>kV</td><td>20</td><td>200</td></tr>
<tr><td>B-dot, nominal/max.</td><td>T/s</td><td>2.15/2.6</td><td></td></tr>
<tr><td>Energy gain, nominal/max.</td><td>keV/turn</td><td>8.3/10</td><td>100</td></tr>
<tr><td>Synchronous phase, nominal</td><td>deg</td><td colspan="2">150</td></tr>
<tr><td>Beam</td><td></td><td></td><td></td></tr>
<tr><td>ε_x; ε_y (at injection)</td><td>$\pi\mu$m</td><td colspan="2">25; 150</td></tr>
<tr><td>Momentum spread, rms</td><td></td><td colspan="2">3×10^{-4}</td></tr>
<tr><td>Polarization at injection</td><td>%</td><td>>75</td><td>100</td></tr>
<tr><td>Radial width of beam (90%), at inj.</td><td>inch</td><td>2.5</td><td>$\sqrt{\beta_x\varepsilon_x/\pi} = 1.1$</td></tr>
</table>

- along the on-momentum closed orbit, and along off-momentum chromatic closed orbits, across a cell;

- along orbits at large horizontal excursion;

- along orbits at large vertical excursion.

For all these cases, verify qualitatively, from the graphs, that $B(s)$ appears as expected.

(d) Justify considering the betatron oscillation as sinusoidal, namely,

$$y(\theta) = A\cos(\nu_y\theta + \phi)$$

wherein $\theta = s/R$, $R = \oint ds/2\pi$.

(e) Produce an acceleration cycle from 50 MeV to 17 GeV about, for a few particles launched on a common $10^{-5}\,\pi$m vertical initial invariant, with small horizontal invariant. Ignore synchrotron motion (CAVITE[IOPT=3] can be used in that case).

Take a peak voltage $\hat{V} = 200\,\mathrm{kV}$ (this is unrealistic but yields 10 times faster computing than the actual $\hat{V} = 20\,\mathrm{kV}$, Tab. 9.2) and synchronous phase $\phi_s = 150\,\mathrm{deg}$ (justify $\phi_s > \pi/2$). Add spin, using SPNTRK, in view of the next question, (f).

Check the accuracy of the betatron damping over the acceleration range, compared to theory. How close to symplectic the numerical integration is (it is by definition *not* symplectic), depends on the integration step size, and on the size of the flying mesh in the DIPOLE method [26, Fig. 20]; check a possible departure of the betatron damping from theory as a function of these parameters.

Produce a graph of the evolution of the horizontal and vertical wave numbers during the acceleration cycle.

(f) Using the raytracing material developed in (e): produce a graph of the vertical spin component of a few particles, and the average value over the 200 particle bunch, as a function of $G\gamma$. Indicate on that graph the location of the resonant $G\gamma_R$ values.

(g) Based on the simulation file used in (f), simulate the acceleration of a single particle, through one particular intrinsic resonance, from a few thousand turns upstream to a few thousand turns downstream.

Perform this resonance crossing for different values of the particle invariant. Determine the dependence of final/initial vertical spin component value, on the invariant value; check against theory.

Re-do this crossing simulation for a different crossing speed. Check the crossing speed dependence of final/initial vertical spin component so obtained, against theory.

(h) Introduce a vertical orbit defect in the ZGS ring.

Find the closed orbit.

Accelerate a particle launched on that closed orbit, from 50 MeV to 17 GeV about, produce a graph of the vertical spin component.

Select one particular resonance, reproduce the two methods of (g) to check the location of the resonance at $G\gamma_R$ =integer, and to find its strength.

References

1. Veksler, V.: A new method of acceleration of relativistic particles. J. of Phys. USSR 9 153-158 (1945)
2. McMillan, E. M.: The Synchrotron. Phys. Rev. 68 143-144 (1945)
3. Goward, F. K., and Barnes, D. E.: Experimental 8 MeV synchrotron for electron acceleration. Nature 158, 413 (1946)
4. Richardson, J.R., et al.: Frequency Modulated Cyclotron. Phys. Rev. 69: 669 (1946)
5. Kerst, D. W.: The Acceleration of Electrons by Magnetic Induction.. Phys. Rev., 60, 47-53 (1941)
6. SATURNE I photos: FAR_SA_N_00248, FAR_SA_N_02826; credit CEA Saclay. Archives historiques CEA. Copyright CEA/Service de documentation
7. Sessler, A., Wilson, E.: Engines of Discovery. A Century of Particle Accelerators. World Scientific, 2007
8. Fig. 9.3: Credit Reider Hahn, Fermilab
9. Endo, K., et al.: Compact proton and carbon ion synchrotrons for radiation therapy. MOPRI087, Proceedings of EPAC 2002, Paris, France; pp. 2733-2735. https://accelconf.web.cern.ch/e02/PAPERS/MOPRI087.pdf
10. Vostrikov, V.A., et al.: Novel approach to design of the compact proton synchrotron magnetic lattice. tupsa17, 26th Russian Particle Accelerator Conference RUPAC2018, Protvino, Russia (2018). https://accelconf.web.cern.ch/rupac2018/papers/tupsa17.pdf
11. Cohen, D, : Feasibility of Accelerating Polarized Protons with the Argonne ZGS. Review of Scientific Instruments 33, 161 (1962).// https://doi.org/10.1063/1.1746524
12. Ratner, L.G. and Khoe, T.K.: Acceleration of Polarized Protons in the Zero Gradient Synchrotron. Procs. PAC 1973 Conference, Washington (1973). http://accelconf.web.cern.ch/p73/PDF/PAC1973_0217.PDF
13. Bywatwr, J., Khoe, T., et al.: A pulsed quadrupole system for preventing depolarization. IEEE Transactions on Nuclear Science (Volume: 20, Issue: 3, June 1973)
14. Cho, Y., et als.: Effects of depolarizing resonances on a circulating beam of polarized protons during or storage in a synchrotron. IEEE Trans. Nuclear Science, Vol.NS-24, No.3, June 1977
15. Parker, E.F.: High Energy Polarized Deuterons at the Argonne National Laboratory Zero Gradient Synchrotron. IEEE Transactions on Nuclear Science, Vol. NS-26, No. 3, June 1979, pp 3200-3202

16. Suddeth, D.E., et als.: Pole face winding equipment for eddy current correction at the Zero Gradient Synchrotron. Procs. PAC 1973 Conference, Washington (1973). http://accelconf.web.cern.ch/p73/PDF/PAC1973_0397.PDF
17. Rauchas, A.V. and Wright, A.J.: Betatron tune profile control in the Zero Gradient Synchrotron (ZGS) using the main magnet pole face windings. Procs. PAC1977 conference, IEEE Trans. on Nucl. Science, VoL.NS-24, No.3, June 1977
18. Floquet, G.: Sur les équations différentielles linéaires à coefficients périodiques. Annales scientifiques de l'E.N.S. 2e série, tome 12 (1883), p. 47-88. http://www.numdam.org/item?id=ASENS_1883_2_12__47_0
19. Leleux, G.: Accélérateurs Circulaires. Lecture Notes, INSTN, CEA Saclay (1978)
20. Leleux, G.: Traversée des résonances de dépolarisation. Rapport Interne LNS/GT-91-15, SATURNE, Groupe Théorie, CEA Saclay (février 1991)
21. Méot, F.: Spin Dynamics. In: Polarized Beam Dynamics and Instrumentation in Particle Accelerators, USPAS Summer 2021 Spin Class Lectures, Springer Nature, Open Acess (2023). https://link.springer.com/book/10.1007/978-3-031-16715-7
22. Lee, S.Y.: Spin Dynamics and Snakes in Synchrotrons. World Scientific, 1997
23. Khoe, T.K., et al.: The High Energy Polarized Beam at the ZGS. Procs. IXth Int. Conf on High Energy Accelerators, Dubna, pp. 288-294 (1974).
Fig. 9.16: Copyrights under license CC-BY-3.0, https://creativecommons.org/licenses/by/3.0; no change to the material
24. Froissart, M. and Stora, R.: Dépolarisation d'un faisceau de protons polarisés dans un synchrotron. Nucl. lnst. Meth. 7 (l960) 297.
25. Bruck H., Debraine P., Levy-Mandel R., Lutz J., Podliasky I., Prevot F., Taieb J., Winter S.D., Maillet R., Caractéristiques principales du Synchrotron Ãă Protons de Saclay et résultats obtenus lors de la mise en route, rapport CEA no.93, CEN-Saclay, 1958.
26. Méot, F.: Zgoubi Users' Guide.
https://www.osti.gov/biblio/1062013-zgoubi-users-guide Sourceforge latest version:
https://sourceforge.net/p/zgoubi/code/HEAD/tree/trunk/guide/Zgoubi.pdf
27. Foss, M.H., et al.: The Argonne ZGS Magnet. IEEE 1965, pp. 377-382, June 1965
28. Klaisner, L.A., et al.: IEEE 1965, pp. 133-137, June 1965

Chapter 10
Strong Focusing Synchrotron

Abstract This Chapter introduces the strong focusing synchrotron, alternating gradient (AG) and separated focusing, and the theoretical material needed for the simulation exercises. It begins with a brief reminder of the historical context, and continues with beam optics, chromaticity, and acceleration. It relies on basic charged particle optics and acceleration concepts introduced in the previous Chapters, and further addresses the following aspects:
- resonances and resonant extraction,
- stochastic energy loss by synchrotron radiation.

The simulation of a strong focusing synchrotron requires just two, possibly three, optical elements from `zgoubi` library: DIPOLE, BEND, or MULTIPOL to simulate (possibly combined function) dipoles, DRIFT to simulate straight sections, and MULTIPOL to simulate lenses (which can be otherwise simulated using QUADRUPO, SEXTUPOL, OCTUPOLE, etc.). A fourth element, CAVITE, is required for acceleration. Particle monitoring requires keywords introduced in the previous Chapters, including FAISCEAU, FAISTORE, possibly PICKUPS, and some others. Spin motion computation and monitoring resort to SPNTRK, SPNPRT, FAISTORE. Optics matching and optimization use FIT[2]. INCLUDE is used, mostly here in order to shorten the input data files. SYSTEM is used to, mostly, resort to gnuplot so as to end simulaitons with some specific graphs obtained by reading data from output files such as zgoubi.fai (resulting from the use of FAISTORE), zgoubi.plt (resulting from IL=2), or other zgoubi.*.out files resulting from a PRINT command.

Notations used in the Text

B; $\mathbf{B}$, $B_{\mathrm{x,y,s}}$	field value; field vector, its components in the moving frame
$B\rho = p/q$; $B\rho_0$	particle rigidity; reference rigidity
C; C_0	orbit length, $C = 2\pi R + \left[\begin{smallmatrix}\text{straight}\\ \text{sections}\end{smallmatrix}\right.$; reference, $C_0 = C(p = p_0)$
E	particle energy
EFB	Effective Field Boundary
f_{rev}, $f_{\mathrm{rf}} = f_{\mathrm{rev}}$	revolution and accelerating voltage frequencies
G	gyromagnetic anomaly, $G = 1.792847$ for proton
G; $K = G/B\rho$	quadrupole gradient; focusing strength
m; m_0; M	mass, $m = \gamma m_0$; rest mass; in units of MeV/c^2
$\mathbf{p}$; p; p_0	momentum vector; its modulus; reference
P_i, P_f	beam polarization, initial, final
q	particle charge
r, R	orbital radius ; average radius, $R = C/2\pi$
s	path variable
v	particle velocity
$V(t)$; $\hat{V}$	oscillating voltage; its peak value
x, x', y, y', l, $\frac{dp}{p}$	horizontal, vertical, longitudinal coordinates in moving frame

α	momentum compaction
α	trajectory angle
$\beta = v/c$; β_0; β_{s}	normalized particle velocity; reference; synchronous
β_{u}	betatron functions ($u:\ x, y, Y, Z$)
$\gamma = E/m_0$	Lorentz relativistic factor
δp	momentum offset or Dirac distribution
Δp	momentum offset
ε	wedge angle
ε_{u}	Courant-Snyder invariant ($u:\ x, r, y, l, Y, Z, s$, etc.)
ϵ_R	strength of a depolarizing resonance
μ_{u}	betatron phase advance, $\mu_{\mathrm{u}} = \int_{\mathrm{period}} ds/\beta_{\mathrm{u}}(s)$ ($u:\ x, y, Y, Z$)
ν_{u}	wave numbers, horizontal, vertical, synchrotron ($u:\ x, y, Y, Z, l$)
ρ, ρ_0	curvature radius; reference
σ	beam matrix
ϕ; ϕ_{s}	particle phase at voltage gap; synchronous phase
ϕ_{u}	betatron phase advance, $\phi_{\mathrm{u}} = \int ds/\beta_{\mathrm{u}}$ ($u:\ x, y, Y, or Z$)
φ	spin angle to the vertical axis

10.1 Introduction

In the very manner that the 1930s-1940s cyclotron, betatron, microtron, weak focusing synchrotron, still in use today, have since essentially not changed in their concepts, design principles, magnet gap profile, today's gap profile, yoke and current coil geometry of combined function alternating-gradient (AG) dipoles remain essentially as patented in 1950 (Fig. 10.1) [1].

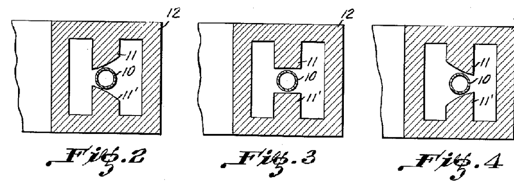

Fig. 10.1 Bending magnet pole profiles for a *focussing system for ions and electrons* [1]. Assuming curvature center to the left, the right (respectively left) profile is defocusing (resp. focusing), the middle profile has zero index

In 1952, in the context of studies relative to the Cosmotron, strong focusing was devised at the Brookhaven National Laboratory (BNL): *"Strong focusing forces result from the alternation of large positive and negative n-values in successive sectors of the magnetic guide field in a synchrotron. This sequence of alternately converging and diverging magnetic lenses* [...] *leads to significant reductions in oscillation amplitude"* [2]. It led to the construction of the first two high-energy proton AG synchrotrons, in the 30 GeV range, in the late 1950s: the proton-synchrotron (PS) at CERN, and the AGS at BNL, major pieces 60 years later still, of the respective injection chains of the two largest colliders in operation, the LHC and RHIC. Early works at BNL provided theoretical formalism, still at work today, for the analyzis of beam dynamics in synchrotrons [3].

The optical principle behind the AG concept is that a doublet of focusing and defocusing lenses with proper stengths results in a, possibly quite strong, very short focal distance, converging system. The dramatic effect of strong-index AG on transverse beam size allows small dipole gaps, thus small magnets: from lowest energies (medical synchrotrons in the 100 MeV range for instance) to the highest ones (particle physics and nuclear physics colliders, hundreds of GeV to multi-TeV range), beams are essentially confined in a centimeter scale transverse space, making a synchrotron a string of dipole magnets containing beam in a ring vacuum pipe of cm to 10 cm diameter; the size of the ring is essentially determined by its circumference, proportional to the magneitc rigidity. This revolutionized the race to high energies, from an upper 10 GeV about of the prior weak focusing synchrotrons and their huge magnets, to todays 7 TeV at the LHC with magnets transverse size in the meter range, and with further plans for 100 TeV rings [5]. It fostered as well the development of high energy synchrotron light sources around the world, with electron beam energies up to 8 GeV.

The original AG dipole design (that of the PS and AGS rings), whereby gradient dipoles combine beam guiding and beam focusing, has the benefit of compactness. It is still prised today and resorted to, for instance in hadrontherapy applications (Fig. 10.3); light source lattice vertical focusing [7], etc. Seperated function AG focusing, whereby beam guiding is ensured by uniform field dipoles while focusing is ensured separately by quadrupoles, followed from the development of the latter

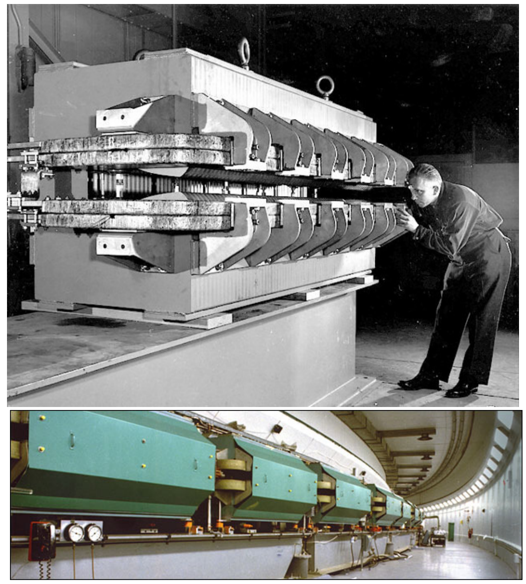

Fig. 10.2 Top: the AGS combined function main magnet - one of 240 steering the beam around the ring, bottom: the 809 m circumference AGS synchrotron [4]. The hyperbolic profile poles are visible on the top photo, partly hidden by the field coils

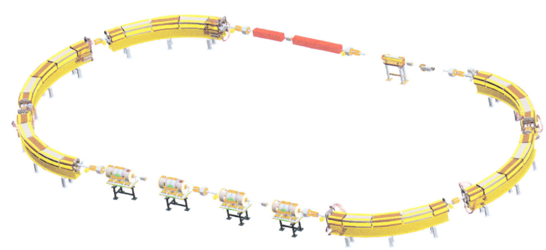

Fig. 10.3 The ion rapid cycling medical synchrotron (iRCMS) [6], an RCS aimed at providing ion beams for the treatment of cancer tumours

(Fig.10.4), a spin-off of the strong index technology [8]. Separated function optics has the merit of flexibility, allowing modular functions in complex rings such as bending-free dispersion suppression sections, low-beta collision or insertion device sections, long straights, etc. Low-emittance, high-brightness light source lattices have complicated focusing further, by introducing longitudinal field gradient bending systems, aimed at minimizing the chromatic invariant [9].

Due to the necessary ramping of the field in order to maintain a constant orbit, synchrotrons accelerators are pulsed, some storage rings species are pulsed as well, high energy colliders in particular to bring beams to highest store energy. The acceleration is cycled and the accelerating voltage fequency as well in ion accelerators, from injection to top energy. If the ramping uses a constant electromotive force, then (Eq. 9.3)

$$B(t) \approx \frac{t}{\tau} \tag{10.1}$$

Fig. 10.4 A quadrupole magnet at LBL in 1957, used for beam lines at the 184-inch cyclotron. An early specimen here, obviously, being a spin-off of the early 1950s concept of strong focusing [10]

$\dot{B} = dB/dt$ does not exceed a few Tesla/second, thus the repetition rate of the acceleration cycle if of the order of a Hertz. If instead the magnet winding is part of a resonant circuit then the field oscillate,

$$B(t) = B_0 + \frac{\hat{B}}{2}(1 - \cos \omega t) \tag{10.2}$$

so that, in the interval of half a voltage repetition period (*i.e.*, $t : 0 \rightarrow \pi/\omega$) the field increases from an injection threshold value to a maximum value at highest rigidity, $B(t) : B_0 \rightarrow B_0 + \hat{B}$. The latter determines the highest achievable energy: $\hat{E} = pc/\beta = q\hat{B}\rho c/\beta$. The repetition rate with resonant magnet cycling can reach a few tens of Hertz, a species known as a rapid-cycling synchrotron (RCS). In both cases anyway B imposes its law and the other quantities comprising the acceleration cycle (RF frequency in particular) will follow B(t).

Rapid cycling allows high intensity beams. Instances are the Cornell 12 GeV, 60 Hz, electron synchrotron, commissioned in 1967, today the injector of Cornell 5 GeV synchrotron light source (CHESS); Fermilab 8 GeV, 60 Hz, booster which provides protons for the production of neutrino beams; the 30 GeV 500 kW beam J-PARC facility in Japan. Rapid cycling is also considered in ion-therapy applications, Fig. 10.3.

10.2 Basic Concepts and Formulæ

Alternating gradient focusing is sketched in Fig. 10.5.

The focusing index value can be estimated from the fields met in these structures: a maximum $B \sim 1$ Tesla in the dipole gap, and as well at pole tip in quadrupoles ~ 10 cm off axis. The latter results in $\frac{\Delta B}{\Delta x} \sim 10$ T/m, the former in ~meters to tens of meters dipole curvature radius. All in all,

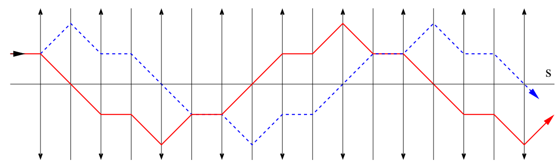

Fig. 10.5 Horizontally focusing lenses (field index $n \gg 0$, the solid red trajectory) are vertically defocusing ($n \ll 0$, the dashed blue trajectory), and vice versa. This imposes alternating gradients in order for a sequence to be globally focusing.

$$n = \frac{\rho}{B}\frac{\partial B}{\partial x} \sim \frac{10^{0\sim 2}_{[\mathrm{m}]}}{1_{[\mathrm{T}]}} \times 10_{[\mathrm{T/m}]} \sim 10^{1\sim 3} \quad \gg 1 \tag{10.3}$$

much greater than in a weak focusing structure, characterized by $0 < n < 1$.

10.2.1 Components of the Strong Focusing Optics

Combined function (AG) optics

This is, typically, the BNL AGS and CERN PS optics, using dipoles that ensure both beam guiding and focusing (Fig. 10.2). Separate quadrupole and multipole lenses have later been introduced in these lattices as they provide knobs for the adjustment of optical functions and parameters.

AG optics is still at work in modern designs, as in th iRCMS whose six 60 deg arcs are comprised of a sequence of five focusing and defocusing combined function dipoles [6], Fig. 10.3.

Field

Referring to the normal conducting magnet technology, an hyperbolic pole profile (Fig. 10.1): equipotential $V(x, y) = A\,xy$ (A a constant, typically $\sim 10\,\mathrm{T/m}$, *cf.* Eq. 10.3), results in $B_y = \frac{\partial V}{\partial y} = A\,x$, *i.e.* a radial field index $n = \frac{\rho}{B_y}\frac{\partial B}{\partial x}|_{\mathrm{y=0}}$, responsible for the focusing; the pole profile opens up either inward (toward the center of curvature, a horizontally focusing dipole, vertically defocusing) or outward (a vertically focusing dipole, horizontally defocusing), Fig. 10.6.

In a straight AG dipole a line of constant field is a straight line; an instance is the AGS main magnet (Fig. 10.2). Another instance is the Fermilab recycler arcs permanent magnet dipole, which includes quadrupole and sextupole components [11, 12]. The modeling of the field can be derived from the Laplace potential $V(s, x, y)$, see below; the AGS on-line model uses that technique [13].

In a bent AG dipole a line of constant field is an arc of a circle; the field guides the reference particle along the arc in the median plane. The mid-plane field can be expressed as

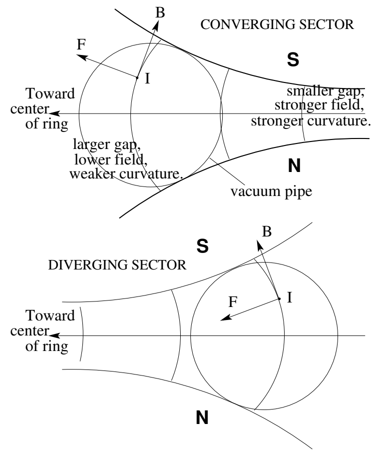

Fig. 10.6 Beam focusing in combined function dipoles. The center of curvature is to the left. The pole profile follows an equipotential $V = axy$. Top: the pole profile opens up towards the center of curvature → the dipole is horizontally converging (vertically diverging: current I comes out of the page, force **F** results from field **B**). Bottom: pole profile closing toward the center of curvature → the dipole is horizontally diverging, vertically converging

$$B_y(r,\theta) = \mathcal{G}(r,\theta)\, B_0 \left(1 + n\,\frac{r-r_0}{r_0} + n_2 \left(\frac{r-r_0}{r_0}\right)^2 + n_3 \left(\frac{r-r_0}{r_0}\right)^3 + \ ...\right) \quad (10.4)$$

with r_0 the eference radius. Higher order indices, sextupole n_2, octupole n_3, ..., may be residual effects: fabrication tolerance, saturation, magnetic permeability, deformation of yoke with years, ..., as in the AGS dipoles, or included by design.

In a straight AG dipole a line of constant field is a straight line; an instance is the AGS main magnet (Fig. 10.2). Another instance is the Fermilab recycler arcs permanent magnet dipole, which includes quadrupole and sextupole components [11, 12]. The modeling of the field in a straight combined function dipole can be derived from the scalar potential of Eq. 10.5.

Separated function optics

Main bends have zero index and ensure beam guiding. In smaller rings though, bending may contribute horizontal focusing; wedge angles in addition may be introduced and contribute some horizontal and vertical focusing/defocusing. Quadrupole lenses, alternately focusing and defocusing, ensure the essential of the focusing.

Higher order multipole lenses are used for the compensation of adverse effects: coupling, aberrations, space charge, impedance, etc., and for beam manipulations: coupling, resonant extraction, etc.

The field in a multipole of order n (n = 1, 2, 3, …: dipole, quadrupole, sextupole, ...) derives, via $\mathbf{B} = \mathbf{grad}V$, from the Laplace potential [14]

$$V_n = (n!)^2 \left\{ \sum_{\mathrm{q=0}}^{\infty} (-)^q \alpha_{\mathrm{n,0}}^{(2q)}(s) \frac{(x^2+y^2)^q}{4^q q!(n+q)!} \right\} \left\{ \frac{x^{n-m} y^m}{m!(n-m)!} \sin m\frac{\pi}{2} \right\} \qquad (10.5)$$

wherein $\alpha_{\mathrm{n},0}^{(2q)} = d^{2q}\alpha_{\mathrm{n},0}/ds^{2q}$ accounts for the s-dependence of the field form factor. Technologies for multipoles and combined multipoles include warm magnets and pole profiling (Figs. 10.2, 10.4), permanent magnets [11, 15], superconducting magnets and $\cos\theta$ windings as in RHIC and LHC colliders, and variants.

In a hard-edge model the left sum in Eq. 10.5 is reduce to the $q = 0$ term, with the following outcomes.

Quadrupole

The equipotential (the pole profile) is an hyperbola: Gxy =constant, in an upright quadrupole (left), $G(x^2 - y^2)$ =constant in a $\pi/4$ skewed quadrupole (right); the resulting field writes

$$B_x = \frac{\partial V}{\partial x} = Gy \qquad B_y = \frac{\partial V}{\partial y} = Gx$$

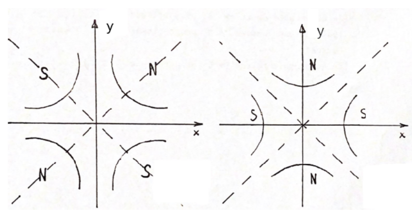

$$B_x = Gx \qquad B_y = -Gy$$

Upright quadrupoles are used for focusing, skew quadrupoles are used to compensate, or introduce, transverse coupling. Their focusing strength

$$K = \frac{1}{L}\frac{\int G(s)\,ds}{p/q}$$

is momentum-dependent.

Sextupole

The equipotential satisfies $H(3x^2y - y^3)$ =constant in an upright sextupole (left), $H(x^3 - 3xy^2)$ =constant in a $\pi/6$ skewed sextupole (right), with resulting field

$$B_x = 2Hxy \qquad B_y = H(x^2 - y^2)$$

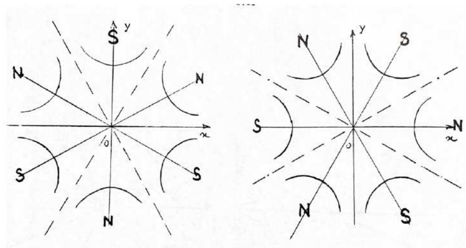

$$B_x = H(x^2 - y^2) \qquad B_y = -2Hxy$$

Upright sextupoles introduce a vertical field component $B_y \propto x^2$, they are used to correct optical aberrations, to modify the momentum dependence of the wave numbers ν_x, ν_y, and in beam manipulations such as resonante extraction. Skew sextupoles introduce a radial field component $B_x \propto y^2$, they are used to correct optical aberrations.

Octupole

The equipotential pole profile satisfies $O(x^3y - xy^3)$ =constant in an upright octupole (left), $O(x^4 - 6x^2y^2 + y^4)$ =constant in a $\pi/8$ skewed octupole (right), yielding the field

$$B_x = O(3x^2y - y^3) \qquad B_y = O(x^3 - 3xy^2)$$

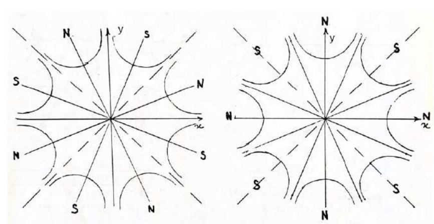

$$B_x = O(x^3 - 3xy^2) \qquad B_y = -O(3x^2y - y^3)$$

Upright octupoles are used to introduce a vertical field componnet $B_y \propto x^3$; skew octupoles introduce a vertical field component $B_y \propto y^3$ Octupoles are used to correct aberrations, or to modify the amplitude dependence of wave numbers.

10.2.2 Transverse motion

The transverse motion of a particle in the periodic lattice of a ring acceleratior satisfies Hill's equations

$$\frac{d^2x}{ds^2} + K_x(s)x = \frac{1}{\rho_0}\frac{\Delta p}{p_0}, \qquad \frac{d^2y}{ds^2} + K_y(s)y = 0 \tag{10.6}$$

wherein $K_x(s)$, $K_y(s)$ have the periodicity of the lattice, and depend locally on the nature of the optical elements:

$$\begin{array}{lll}
- \text{ dipole :} & \begin{cases} K_x = \dfrac{1-n}{\rho_0^2} \\ K_y = \dfrac{n}{\rho_0^2} \end{cases} & (n = -\frac{\rho_0}{B_0}\frac{\partial B_y}{\partial x}) \\
- \text{ a wedge at } \mathrm{s} = \mathrm{s}_0 : & \Big\{ K_{\substack{x\\y}} = \pm\dfrac{\tan\varepsilon}{\rho_0}\delta(s-s_0) \ \left(\varepsilon \lesseqgtr 0 : \begin{array}{l}\text{focusing}\\ \text{defocusing}\end{array}\right); \ \frac{1}{\rho_0} = 0 & \\
- \text{ quadrupole} & (\text{gradient } G = \frac{\text{field at pole tip}}{\text{radius at pole tip}}) : K_{\substack{x\\y}} = \dfrac{\pm \mathrm{G}}{B\rho}; \ \dfrac{1}{\rho_0} = 0 & \\
- \text{ drift space :} & K_x = K_y = 0; \ \dfrac{1}{\rho_0} = 0 &
\end{array} \tag{10.7}$$

By contrast with the single index ($0 < n < 1$) betatron and weak focusing technologies, strong focusing with its independent focusing ($G > 0$) and defocusing ($G < 0$) families allows separate adjustment of the horizontal and vertical focusing strengths, and wave numbers as a consequence.

The on-momentum ($p = p_0$) closed orbit coincides with the reference axis of the optical structure. The betatron motion for an on-momentum particle, *i.e.* the excursion x, y around the closed orbit, satisfies Eq. 10.6 with $\Delta p = 0$. Solving the latter (see Sect. 9.2) requires introducing two independent solutions $u_{\substack{1\\2}}(s)$ (Eq. 9.12), the linear combination of which yields the pseudo harmonic motion (Eq. 9.15)

$$\left| \begin{array}{l} u(s) = \sqrt{\beta(s)\varepsilon/\pi}\, \cos\left(\int \dfrac{ds}{\beta(s)} + \varphi\right) \\ u'(s) = -\sqrt{\dfrac{\varepsilon/\pi}{\beta(s)}}\, \sin\left(\int \dfrac{ds}{\beta(s)} + \varphi\right) + \alpha(s)\, \cos\left(\int \dfrac{ds}{\beta(s)} + \varphi\right) \end{array} \right. \tag{10.8}$$

The motion satisfies the Courant-Snyder invariant, namely (Fig. 9.10)

$$\gamma_u(s)u^2 + 2\alpha_u(s)uu' + \beta_u(s)u'^2 = \frac{\varepsilon_u}{\pi} \tag{10.9}$$

The form and the orientation of this phase space ellipse change along the period, its surface is constant.

Beam envelopes are given by the extrema,

$$\hat{x}_{\text{env}}(s) = \pm\sqrt{\beta_x(s)\frac{\varepsilon_x}{\pi}}, \qquad \hat{y}_{\text{env}}(s) = \pm\sqrt{\beta_y(s)\frac{\varepsilon_y}{\pi}} \tag{10.10}$$

Phase space motion

Write the two independent solutions $u_{\frac{1}{2}}(s)$ (Eq. 9.12) under the form

$$u_1(s) = \underbrace{F(s)}_{\text{S−periodic}} \times \underbrace{e^{i\mu\frac{s}{S}}}_{\frac{2\pi S}{\mu}\text{−periodic}} \quad \text{and} \quad u_2(s) = u_1^*(s) = F^*(s)\, e^{-i\mu\frac{s}{S}} \tag{10.11}$$

wherein $F(s) = \sqrt{\beta(s)}\, e^{i\left(\int_0^s \frac{ds}{\beta(s)} - \mu\frac{s}{S}\right)}$. Introduce $\psi(s) = \int_0^s \frac{ds}{\beta(s)} - \mu\frac{s}{S}$ so that $F(s) = \sqrt{\beta(s)}\, e^{i\psi(s)}$, Eq. 10.8 thus takes the form

$$\left|\begin{array}{l} u(s) = \overbrace{\sqrt{\beta(s)\varepsilon/\pi}}^{S\text{−periodic}}\ \overbrace{\cos\left[\nu\frac{s}{R} + \underbrace{\psi(s)}_{\text{S−per.}} + \varphi\right]}^{\frac{2\pi S}{\mu}\text{−periodic}} \\ u'(s) = -\sqrt{\frac{\varepsilon/\pi}{\beta(s)}}\ \sin\left[\nu\frac{s}{R} + \psi(s) + \varphi\right] + \alpha(s)\ \cos\left[\nu\frac{s}{R} + \psi(s) + \varphi\right] \end{array}\right. \tag{10.12}$$

wherein $\nu = \frac{N\mu}{2\pi}$. Thus, as $\beta(s)$ and $\psi(s)$ are S-periodic functions, the turn-by-turn motion observed at a given azimuth s (*i.e.*, $u(s)$, $u(s+\mathcal{S})$, $u(s+2\mathcal{S})$, ...) is sinusoidal with frequency $\nu = N\mu/2\pi$. Successive particle positions $(u(s), u'(s))$ in phase space lie on the Courant-Snyder invariant (Eq. 10.9).

The wave numbers ν_x and ν_y can be adjusted independently in a separated function lattice, by means of two independent quadrupole families. The working point (ν_x, ν_y) fully characterizes the first order optical setting of the ring.

Off-momentum motion

The motion of an off-momentum particle satisfies the inhomogeneous Hill's horizontal differential Eq. 10.6. The chromatic closed orbit

$$x_{\text{ch}}(s) = D_x(s)\frac{\delta p}{p} \tag{10.13}$$

is a particular solution of the equation, its periodicity is that of the cell.

By contrast with the weak focusing configuration, where the on-momentum closed orbit and chromatic closed orbits are parallel (Eq. 9.26: D_x=constant, independent of s), chromatic closed orbits in a strong focusing optical structure are distorted, their excursion depends on the distribution along the cell of (i) the dispersive elements which are the dipoles, and (ii) the focusing.

The horizontal motion of an off-momentum particle is a superposition of the particular solution (Eq. 10.13) and of the betatron motion, solution of the homogeneous Hill's equation (Eq. 9.22 with $\delta p/p = 0$), namely

$$x(s) = x_\beta(s) + x_{\mathrm{ch}}(s) = \sqrt{\beta_x(s)\frac{\varepsilon_x}{\pi}}\ \cos\left(\int \frac{ds}{\beta_x} + \varphi\right) + D_x(s)\frac{\Delta p}{p_0} \tag{10.14}$$

whereas the vertical motion is unchanged (Eq. 10.12 taken for $u(s) \equiv y(s)$).

10.2.3 Resonances. Resonant Extraction

Consider the excitation of transverse beam motion by a generator of frequency Ω located at some azimuth along the ring [16]. The action of the excitation $S \times \sin\Omega t$ on the oscillating motion $u(t)$ can be written under the form

$$\frac{d^2u}{dt^2} + \omega^2 u = S\sin\Omega t \tag{10.15}$$

The betatron motion is assumed harmonic for simplicity, case for instance of weak focusing. Take S constant, the solution (superposition of the solution of the homogeneous differential equation and of a particular solution of the inhomogeneous differential equation) writes

$$u(t) = U\cos(\omega t + \varphi) + \frac{S}{\omega^2 - \Omega^2}\sin\Omega t \tag{10.16}$$

If betatron motion and excitation are in synchronism, *i.e.* on the resonance, $\omega = \Omega$, a particular solution of Eq. 10.15 is

$$u_r(t) = -\frac{S\,t}{2\Omega}\cos\Omega t$$

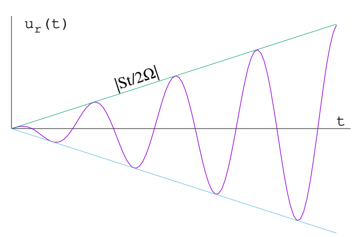

the amplitude of the oscillatory motion grows rapidely with time, at a rate $|St/2\Omega|$.

Assume S periodic instead, take its Fourier expansion $S(t) = \sum_{p=0}^{\infty} a_p \cos(p\omega' t + \varphi_p)$, the equation of motion thus writes

$$\frac{d^2u}{dt^2} + \omega^2 u = \sum_{p=0}^{\infty} a_p \cos(p\omega' t + \varphi_p)\ \sin\Omega t =$$

$$\sum_{p=0}^{\infty} \frac{a_p}{2} \Big[\sin[(\Omega - p\omega')t + \varphi_p] + \sin[(\Omega + p\omega')t + \varphi_p] \Big]$$

Resonance may occur at oscillator frequencies $\omega = \Omega \pm p\omega'$, their strength depends on the amplitude a_p of the excitation harmonics. If the generator is located at one point in the ring, it excites all harmonics.

Sextupole and octupole resonances

The horizontal motion in the presence of a sextupole component ($B_y(\theta)|_{y=0} = S(\theta)x^2$, see *Sextupole*, above) as part of the ring optical lattice satisfies

$$\frac{d^2x}{d\theta^2} + \nu_x^2 x = S(\theta)x^2 \tag{10.17}$$

Assume weak perturbation of the motion, so that $x(\theta) \approx \hat{x}\cos(\nu_x\theta + \varphi)$; the perturbation $S(\theta)$ is 2π-periodic thus substitute its Fourier series expansion $S(\theta) = \sum_{p=0}^{\infty} a_p \cos(p\omega'\theta + \varphi_p)$ in the differential equation; develop to get

$$\frac{d^2x}{d\theta^2} + \nu_x^2 x = \frac{\hat{x}^2}{2} \sum_{\mathrm{p}=0}^{\infty} a_p \Big[\cos(p\theta + \varphi_p) +$$

$$\cos[(p - 2\nu_x)\theta + \varphi_p - 2\varphi] \ + \ \cos[(p + 2\nu_x)\theta + \varphi_p + 2\varphi] \Big]$$

Thus resonance may occur at betatron frequency families $\nu_x = \pm p$, $\nu_x = \pm(p - 2\nu_x)$, and $\nu_x = \pm(p + 2\nu_x)$, *i.e.*,

$$\left[\begin{array}{l} \nu_x = \text{integer} \\ 3\nu_x = \text{integer} \end{array} \right.$$

In the case of a single sextupole in the ring, all the harmonics p are excited with the same amplitude a_p.

An octupole perturbation introduces a field component $B_y(\theta)|_{y=0} = O(\theta)x^3$ (see *Octupole*, above) in the optical lattice. In a similar way, assume weak perturbation so that $x(\theta) \approx \hat{x}\cos(\nu_x\theta + \varphi)$; to $O(\theta)$ substitute its Fourier expansion; this yields

$$\left[\begin{array}{l} \nu_x = \text{integer} \\ 2\nu_x = \text{integer} \\ 4\nu_x = \text{integer} \end{array} \right.$$

Resonances in a general manner occur at betatron frequencies satisfying

$$m\nu_x + n\nu_y = \text{integer}$$

with the property that

$$\frac{\varepsilon_x}{m} - \frac{\varepsilon_y}{n} = \text{constant}, \qquad \text{an invariant of the motion}$$

with the following consequences:

- if m and n have opposite signs the resonance causes energy exchange betwen the horizontal and vertical motions: $\frac{\varepsilon_x}{|m|} + \frac{\varepsilon_y}{|n|}$ = constant, an increase of ε_x correlates with a decrease of ε_y and vice-versa; in the presence of linear coupling for instance, $\nu_x - \nu_y$ = integer, $\varepsilon_x + \varepsilon_y$ = constant; an increase in motion amplitude anyway may cause particle loss, an issue in cyclotrons with the Walkinshaw resonance $\nu_x = 2\nu_y$ which causes vertical beam loss upon increase of ε_y;

- if m and n have the same sign the resonance induces motion instabilty: $\frac{\varepsilon_x}{m} - \frac{\varepsilon_y}{n}$ = constant, ε_x and ε_y may both increase with no limit.

Resonant Extraction

10.2.4 Synchrotron Motion

Paticle motion in the longitudinal phase space (phase, momentum) is determined by the lattice and by the acceleration parameters. The synchrotron acceleration technique has been discussed in Sect. 9.2.2, outcomes are leaned on, here.

Acceleration parameters include RF voltage $\hat{V}$, frequency $f_{\rm rf} = \omega_{\rm rf}/2\pi$, ******* Transition $\gamma_{\rm tr}$ is a property of the lattice and determines the synchronous phase region, $[0, \pi/2]$ or $[\pi/2, \pi]$.

Synchrotron angular frequency

$$\Omega_s = (\omega_{\rm rev}^2\, |\eta| h_{\rm RF} e\hat{V} \cos\phi_s \;/\; 2\pi E_s)^{1/2}$$

with $\eta = 1/\gamma^2 - \alpha$ the phase slip factor (Eq. 9.33), $h_{\rm RF}$ the RF harmonic, $\omega_{\rm rev} = 2\pi/T_{\rm rev}$ the revolution angular frequency, $\hat{V}$ the RF peak voltage, ϕ_s the synchronous phase.

The bucket height, “momentum acceptance”, satisfies

$$\pm\frac{\Delta p}{p} = \pm\frac{1}{\beta}\sqrt{\frac{q\hat{V}}{\pi h \eta E_s}\left[-(\pi - 2\varphi_s)\sin\varphi_s + 2\cos\varphi_s\right]} \tag{10.18}$$

$$\alpha = \frac{\Delta C}{C}\bigg/\frac{\Delta p}{p_0} \equiv \frac{\Delta R}{R}\bigg/\frac{\Delta p}{p_0} \tag{10.19}$$

The maximum extent in phase for small amplitude oscillations satisfies

$$\pm\Delta\varphi_{\rm max} = \frac{h\eta E_s}{p_s R_s \Omega_s} \times max\left(\frac{\Delta E}{E_s}\right) \tag{10.20}$$

****** separatrix **********

The motion of a particle with enegy offset $\delta E = E - E_s$ satisfies the longitudinal invariants

$$\epsilon_l = \frac{\alpha E_s}{2\Omega_s}\left[\left(\frac{\delta E}{E_s}\right)^2 + \frac{1}{\Omega_s^2}\left(\frac{d}{dt}\frac{\delta E}{E_s}\right)^2\right] \tag{10.21}$$

$$(\widehat{\delta E})^2 = (\delta E)^2 + \frac{1}{\Omega_s^2}\left(\frac{d\delta E}{dt}\right)^2 \tag{10.22}$$

Introducing the squared *rms* relative synchrotron amplitude $\sigma^2_{\widehat{\delta E}/E} \equiv (\widehat{\delta E}/E_s)^2$ this yields in addition

$$\epsilon_l = \frac{\alpha E_s}{2\,\Omega_s}\,\sigma^2_{\widehat{\delta E}/E} \tag{10.23}$$

10.2.5 Radiative Energy Loss

check what was said in betatron chapter ...

A particle of rest mass m_0 and charge e travelling in a magnetic field is subject to stochastic photon emission, which causes energy loss [19]. The phenomenon involves two random processes:

- the probability of photon emission over a trajectory arc δs, a Poisson law,

$$p(k) = \frac{\Lambda^k}{k!}e^{-\Lambda} \qquad \text{with} \quad \Lambda =< k >=< k^2 > \tag{10.24}$$

wherein k is the number of photons emitted over δs, $\Lambda = \frac{5er_0}{2\hbar\sqrt{3}}B\rho\frac{\delta s}{\rho}$ is its average value, $r_0 = e^2/\,4\pi\epsilon_0 m_0 c^2$ is the classical radius of the particle, $\epsilon_0 = 1\,/\,36\pi 10^9$, $\hbar$ is the Plank constant,

- the energy ϵ of the photon(s), following the probability law

$$\mathcal{P}\left(\frac{\epsilon}{\epsilon_c}\right) = \frac{3}{5\pi}\int_0^{\epsilon/\epsilon_c}\frac{d\epsilon}{\epsilon_c}\int_{\epsilon/\epsilon_c}^{\infty} K_{5/3}(x)dx \tag{10.25}$$

with $K_{5/3}$ the modified Bessel function, $\gamma = E/E_0$ with $E_0 = m_0c^2$ the rest energy, and ϵ_c the critical energy of the radiation,

$$\epsilon_c = \frac{3\hbar\gamma^3 c}{2\rho} \tag{10.26}$$

The average energy loss over δs is, assuming ultra-relativistic particles: $\beta = v/c \approx 1$,

$$\delta E = \frac{2}{3}r_0 E_0\gamma^4\,\frac{\delta s}{\rho^2} = \frac{2}{3}r_0 ec\gamma^3 B\frac{\delta s}{\rho} \quad \underbrace{\approx 1.88\ 10^{-15}\ \gamma^3\frac{\delta s}{\rho^2}}_{\text{for electrons}} \tag{10.27}$$

The energy spread resulting from the stochastic emission is

$$\sigma_{\delta E/E} = \frac{\sqrt{110\sqrt{3}\hbar c\ /\ \pi\epsilon_0}}{24E_0/e}\,\gamma^{5/2}\,\frac{\sqrt{\delta s}}{\rho^{3/2}}\quad \underbrace{\approx 3.80\ 10^{-14}\ \gamma^{5/2}\frac{\sqrt{\delta s}}{\rho}}_{\text{for electrons}} \tag{10.28}$$

In a storage ring the RF system restores on average the energy lost by SR. Usefull formulas are given in Tab. 10.1, in particular, assuming a flat ring the partition of energy between radial and longitudinal motions is determined by the partition numbers

$$\mathrm{J_x} = 1-\mathcal{D},\ \ \mathrm{J_y} = 1,\ \ \mathrm{J_l} = 2+\mathcal{D},\ \ \text{with } \mathcal{D} = \frac{\overline{\mathrm{D_x}(1-2\mathrm{n})/\rho^3}}{\overline{\rho^2}} \tag{10.29}$$

where $\overline{(*)}$ denotes an average over the ring circumference.

Table 10.1 Radiation parameters$^{(a)}$, energy loss and equilibrium quantities at the synchronous energy, E_s, in an isomagnetic ring

Critical photon energy, ϵ_c	keV	$\frac{3\hbar\gamma^3 c}{2\rho}$
Average photon energy, $\overline{\epsilon}$	keV	$\frac{8}{15\sqrt{3}}\epsilon_c$
rms energy spread, $\sqrt{\overline{(\epsilon-\overline{\epsilon})^2}}$	keV	$\frac{\sqrt{211}}{15\sqrt{3}}\epsilon_c$
Energy loss, U_s	MeV / turn	$C_\gamma\frac{E_s^4}{\rho}$
Nb. of average photons	/turn/particle	$U_s/\overline{\epsilon}$
Longitudinal:		
equil. emittance, $\varepsilon_{l,eq}$	μeV.s	$\frac{\alpha E_s}{\Omega_s}\frac{C_q\gamma^2}{J_l\,\rho}$
rms energy spread, $\sigma_{\delta E/E}$		$\frac{1}{\sqrt{2}}\sigma_{\widehat{\delta E}/E} = \sqrt{\frac{C_q}{J_l\rho}}\gamma$
rms bunch length, σ_l	mm	$\frac{\alpha c}{\Omega_s}\sigma_{\frac{\delta E}{E}}$
Radial:		
equil. emittance, $\varepsilon_{x,eq}$	nm	$= \frac{C_q\gamma^2}{J_x\rho}\bar{\mathcal{H}}$
rms width, $\sigma_x(s)^{(b)}$	m	$\left(\beta_x(s)\varepsilon_{x,eq} + D_x^2(s)\sigma^2_{\frac{\delta E}{E}}\right)^{1/2}$
Damping times, $\tau_{x,y,l}$	ms	$\frac{T_{rev}E_s}{U_sJ_{x,y,l}}$

(a) Units are, c: m/s; ρ: m; E_s: GeV
$C_\gamma = \frac{4\pi}{3}\frac{r_0}{(m_0c^2)^3}$ (= 8.846276 10^{-5} m/GeV^3 for electrons).
$C_q = \frac{55}{32\sqrt{3}}\frac{\hbar}{m_0c}$ (= 3.8319386×10^{-13} m for electrons).
(b) With $\varepsilon_{x,eq}, \beta(s)$ and dispersion $D_x(s)$ in meter.

Damping of accelerated motion

In an accelerator (a light source injector for instance), the RF voltage increases during acceleration in order to compensate the increasing energy loss. To first order in the invariant ε_u (with u standing for x or y) transverse damping in the presence of acceleration satisfies [**?**]

$$\frac{d\varepsilon_u}{dt} = -\frac{2}{\tau_u(t)}\varepsilon_u + C_u(t) - \frac{1}{p}\frac{dp}{dt}\varepsilon_u\ , \text{ where } \tau_u^{-1} = J_u\frac{\overline{P}}{2E},\ \begin{cases} C_x = \overline{\mathcal{H}\frac{\dot{N}<\epsilon^2>}{E^2}} \\ C_y = \overline{\frac{\beta_y}{2\gamma^2}\frac{\dot{N}<\epsilon^2>}{E^2}} \end{cases} \tag{10.30}$$

Longitudinal damping satisfies

$$\frac{d(\widehat{\delta E})^2}{dt} = -\frac{2(\widehat{\delta E})^2}{\tau_l(t)} + (\dot{N}\left\langle\epsilon^2\right\rangle)(t) + \frac{(\widehat{\delta E})^2}{2E}\frac{dE_s}{dt} \quad \text{with } \tau_l^{-1} = J_l\frac{\overline{U_s}}{2E_s} \tag{10.31}$$

******** Figures **??**, **??** display the evolution of horizontal and vertical emittance with time, respectively

$$\overline{\epsilon}_\mathrm{x}(\mathrm{t}) = \epsilon_{\mathrm{x},0}\left(\mathrm{e}^{\mathrm{t}/|\tau_\mathrm{x}|} - 1\right), \qquad \overline{\epsilon}_\mathrm{y}(\mathrm{t}) = \epsilon_{\mathrm{y,i}}\,\mathrm{e}^{-\mathrm{t}/\tau_\mathrm{y}} \tag{10.32}$$

with $\epsilon_{\mathrm{x},0}$ a constant and $\epsilon_{\mathrm{y,i}}$ an initial value.

10.2.6 Depolarizing esonances

By contrast with weak focusing optics where depolarizing resonances are weak because horizontal field components are weak (Sect. 9.2.3), the use of stong focusing field gradients in the combined function magnets and/or focusing lenses of strong focusing optics results in strong radial field components and therefore strong depolarizing resonances.

Spin precession and resonant spin motion in the magnetic components of a cyclic accelerator have been introduced in Sects. 4.2.5, 5.2.5. The general conditions for depolarizing resonance to occur have been introduced in Sect. 9.2.3. In a strong focusing synchrotron they assentially result from the radial field components in the focusing magnets and their strength is determined by the lattice optics, as follows.

Strength of imperfection resonances

Imperfection, or integer, depolarizing resonances are driven by a non-vanishing vertical closed orbit $y_{co}(\theta)$ which causes spins to experience periodic radial fields in focusing magnets, dipoles in combined function lattices and quadrupoles in separated function lattices, namely,

$$B_x(\theta) = G\,y(\theta) = K(\theta) \times B_0\rho_0 \times y_{co}(\theta)$$

with θ the orbital angle, $B_0\rho_0$ the lattice rigidity and $y_{co}(\theta)$ the closed orbit excursion. Resonance occurs if the spin undergoes an integer number of precessions over a turn (it then undergoes 1-turn-periodic torques), so that spin tilts at field perturbations along the closed orbit add up coherently. Thus resonances occur at integer values

$$G\gamma_n = n$$

A Fourier development of these perturbative fields yields the strength of the $G\gamma_n$ harmonic [21, Sect. 2.3.5.1]

$$\epsilon_n^{\text{imp}} = (1 + G\gamma)\frac{R}{2\pi} \oint K(\theta)\; y_{co}(\theta)\, e^{-jG\gamma(\theta-\alpha)}\, e^{jn\theta}\, d\theta$$

In the thin-lens approximation this simplifies into a series over the quadrupole fields,

$$\epsilon_n^{\text{imp}} = \frac{1 + G\gamma_n}{2\pi} \sum_{\text{Qpoles}} [\cos G\gamma_n\, \alpha_i + \sin G\gamma_n\, \alpha_i]\, (KL)_i\;\, y_{co}(\theta_i) \tag{10.33}$$

with θ_i the quadrupole location, $(KL)_i$ the integrated strength (slice the dipoles as necessary in an AG lattice for this series to converge) and α_i the cumulated orbit deviation.

Orbit harmonics near the betatron tune ($n = G\gamma_n \approx \nu_y$) excite strong resonances. Imperfection resonance strength is further amplified in P-superperiodic rings, with m-cell superperiods, if the betatron tune $\nu_y \approx$ integer $\times\, m \times P$ [22, Chap.3-I].

Strength of imperfection resonances

Intrinsic depolarizing resonances are driven by betatron motion, which causes spins to experience strong radial field components in quadrupoles, namely

$$B_x(\theta) = G\,y(\theta) = K(\theta) \times B_0\rho_0 \times y_\beta(\theta) \tag{10.34}$$

The effect of resonances on spin depends upon betatron amplitude and phase, their effect on beam polarization depends on beam emittance. Longitudinal fields from dipole ends are usually weak by comparison and ignored. The location of intrinsic resonances depends on betatron tune, it is given in an M-periodic structure by

$$G\gamma_n = nM \pm \nu_y$$

10.3 Exercises

In complement to the present exercises, an extensive tutorial on depolarizing resonances in a strong focusing synchrotron, considering poton, helion, or electron beams, using the lattice of the AGS Booster at BNL, can be found in Ref. [21, Chap. 14,"Spin Dynamics Tutorial: Numerical Simulations"]. The simulaitons include tune-jump quadrupoles, solenoid, snakes, electron beam polaization life time and spin rotators.

10.1 Construct SATURNE II synchrotron. Spin Dynamics With Snakes
Solution: page 361

Over the years 1978-1997 the 3 GeV synchrotron SATURNE II at Saclay (Fig. 10.7) delivered ion beams up to 1.1 GeV/nucleon, including polarized proton, deuteron and ^{6}Li beams, for intermediate energy nuclear physics research, including meson production [17, 18]. The separated function synchrotron was designed *ab initio* for the acceleration of polarized beams [20], and the first strong focusing synchrotron to do so - ZGS, first to accelerate polarized beams, protons and deuterons, was a weak focusing synchrotron (see Chap. 9).

SATUNE II is a FODO lattice with missing dipole. Its parameters are given in Tab. 10.2.

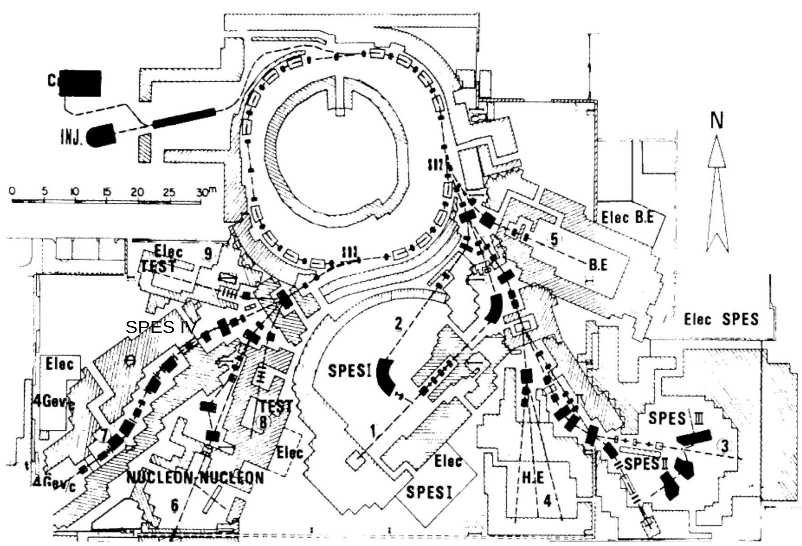

Fig. 10.7 SATURNE II synchrotron and its experimental areas [23], including mass spectrometers SPES I to SPES IV, a typical 1960-80s nuclear physics accelerator facility. Polarized ion sources are on the top left, followed by a 20 MeV linac

(a) Simulate the main dipole using BEND, include fringe fields assuming $\lambda = 8$ cm extent and the following Enge coefficient values (Eq. 15.13, Sect. 15.2.6):

Table 10.2 Parameters of SATURNE II separated function FODO lattice. ρ_0 denotes the reference bending radius in the main dipole; the reference orbit, wave numbers, etc., are taken along that radius

Orbit length, C	m	105.5556
Average radius, $R = C/2\pi$	m	16.8
Length of long straight section	m	
Wave numbers, ν_x; ν_y		3.64; 3.60
Chromaticities, ξ_x; ξ_y		negative, a few units
Momentum compaction α		0.015
Injection energy (proton)	MeV	20
Top energy	GeV	3
$\dot{B}$	T/s	4.2
Synchronous energy gain	keV/turn	1.160
RF harmonic		2
Dipole:		
- bend angle, α	deg	$\pi/8$
- magnetic length, $\rho\alpha$	m	2.489
- magnetic radius, ρ	m	6.3381
- wedge angle, ε	deg	2.45
Quadrupole:		
- gradient	T/m	0.5 - 10.56
- magnetic length F/D	m	0.46723 / 0.486273

$$C_0 = 0.2401,\ C_1 = 1.8639,\ C_2 = -0.5572,\ C_3 = 0.3904,\ C_4 = C_5 = 0$$

Produce a graph of the field across the dipole along the reference orbit, in the median pnae and at 5 cm vertical distance. Produce the transport matrix, check against theory. Compare with the matrix of the hard edge model.

Simulate the F and D quadrupoles, using respectively QUADRUPOLE and MULTIPOL. Compare matrices with theory.

Construct the cell. Produce machine parameters (tunes, chromacities), check against data, Tab. 10.2.

Construct the 4-cell ring. Produce a graph of the optical functions.

(b) Accelerate a bunch with Gaussian densities comprised of a few tens of particles (it can be defined using MCOBJET), from injection to top energy; use harmonic 3 RF frequency, and (unrealistic, for a reduced number of turns) peak RF voltage $\hat{V} = 1$ MV.

Produce a graph of the three phase spaces. Check the transverse betatron damping.

(c) Simulate multiturn injection in the ring. Take the injection point at the center of a long straight section.

(d) Simulate resonant extraction from the ring, on $\nu_x = 11/3$. Take the extraction point at the center of a long straight section.

10.2 Depolarizing Resonances In SATURNE II

The input data file to simulate the ring is given in Tab. 17.73, an outcome of exercise 10.1.

(a) Calculate the strength of the intrinsic depolarizing resonances (systematic and non-systematic) over 0.5-3ǴeV, using Eq. **??**.

(b) Ggamma=7-ν_y was found to be a potentially harmful depolarizing resonance - unexpectedly as this is not a systematic resonance. Produce a crossing of that resonance, for a 100-particle bunch. Get its strength from this simulation, compare with (a).

(c) Multiple resonance xing - ref to Phys. Rev. article ***

10.3 Cornell electron RCS. Radiative Energy Loss

Short intro .... energy loss by synchrotron radiation [24]

Tab.: RCS parameter list

(a) Cornell RCS parameters are given in Tab. **??**. Construct the ring, produce its optical parameters. Poduce a graph of the optical functions.

(b) Raytrace a few tens of particles over 3000 turns in Cornell RCS, from *** to *** GeV. Assume emittances epsilx=, epsily=, Gaussian densities, initial *rms* $\delta p/p = 10^{-4}$. Produce a graph of the three phase spaces. produce graphs of horizontal and vertical transverse excursions versus turn number.

(c) Re-do (b) with synchrotron radiation energy loss.

(d) Produce the average beam polarization obtained in (c).

(c) Multiple resonance crossing.

References

1. Christofilos, Nicholas: Focussing system for ions and electrons. US Patent Office Application filed March 10, 1950, Serial No. 148,920.
   https://patentimages.storage.googleapis.com/fa/bb/52/0ce28e28b492a6/US2736799.pdf
2. Courant, Ernest D., Livingston, M. Stanley, and Snyder, Hartland S.: The Strong-Focusing Synchroton - A New High Energy Accelerator. Phys. Rev. 88, 1190 - December 1952
3. Courant, E. D., and Snyder, H. S.: Theory of the Alternating-Gradient Synchrotron. Annals of Physics, No. 3 (1958), 1âĂŞ48
4. Credit: Brookhaven National Laboratory.
   https://www.flickr.com/photos/brookhavenlab/8495311598/in/album-72157611796003039/
5. I. Agapov, et al.: Future Circular Lepton Collider FCC-ee: Overview and Status. Submitted on 15 Mar 2022; arXiv:2203.08310 [physics.acc-ph].
   https://doi.org/10.48550/arXiv.2203.08310
6. Méot, F., et al.: Progress on the optics modeling of BMIâĂŹs ion rapid-cycling medical synchrotron at BNL. THPMP050, 10th Int. Particle Accelerator Conf. IPAC2019, Melbourne, Australia. https://accelconf.web.cern.ch/ipac2019/papers/thpmp050.pdf
   Copyrights under license CC-BY-3.0, https://creativecommons.org/licenses/by/3.0; no change to the material
7. Nishimori, N.: A new compact 3 GeV light source in Japan. 13th Int. Particle Acc. Conf. IPAC2022, Bangkok, Thailand.
   https://accelconf.web.cern.ch/ipac2022/papers/thixsp1.pdf
8. Radial Focusing in the Linear Accelerator. Phys. Rev. Vol. 88, Num. 5, Dec. 1, 1952
9. BenabderrahmaneâĂă, C.: Status of the ESRF-EBS magnets. WEPMK009, 9th International Particle Accelerator Conference, IPAC2018, Vancouver, BC, Canada.
   https://accelconf.web.cern.ch/ipac2018/papers/wepmk009.pdf
10. Credit: Lawrence Berkeley National Laboratory. The Regents of the University of California, Lawrence Berkeley National Laboratory."
11. Jackson, G., Editor: Fermilab recycler ring technical design report. Rev. 1.1. FERMILAB-TM-1981 (July 1996).
    http://inspirehep.net/record/424541/files/fermilab-tm-1981.PDF
12. Méot, F.: On the Effects of Fringe Fields in the Recycler Ring. FERMILAB-TM-2016 (Aug. 1997).
    http://inspirehep.net/record/448603/files/fermilab-tm-2016.PDF
13. Ahrens, L., et al.: Development of a stepwise ray-tracing based on-line model at the AGS. WEP141, Proceedings of 2011 Particle Accelerator Conference, New York, NY, USA.
    https://accelconf.web.cern.ch/PAC2011/papers/wep141.pdf
14. Leleux, G.: Compléments sur la Physique des Accélérateurs. DEA “Physique et Technologie des Grands Instruments”, Université Paris VI. Rapport interne LNS//86-101, CEA Saclay (1986)
15. F. Méot, et al.: Beam dynamics validation of the Halbach Technology FFAG Cell for Cornell-BNL Energy Recovery Linac. Nuclear Inst. and Methods in Physics Research, A 896 (2018) 60âĂŞ67
16. Leleux, G.: Accélérateurs Circulaires. INSTN lectures, internal report CEA Saclay (1978), unpublished
17. The 20 Years of the Synchrotron SATURNE-2. In: Proceedings of the Colloquium, Paris, France, 04 - 05 May 1998, A. Boudard and P.-A. Chamouard Editors. Edited By CEA - Laboratoire National SATURNE & CEN Saclay, France.
    https://doi.org/10.1142/3965
18. Plus d’anneaux autour de SATURNE (pp. 33-34) Published in: Courrier CERN Volume 39, NÂř 2, Mars 1999.
    https://cds.cern.ch/record/1740121
19. Hofmann, A.: The Physics of Synchrotron Radiation. Cambridge Monographs on Particle Physics, Nuclear Physics and Cosmology (20), Cambridge University Press (2004)

20. E. Grorud, J.L. Laclare and G. Leleux: Crossing of Depolarization Resonances in Strongly Modulated Structures. IEEE Transactionson NuclearScience,Vol. NS-26,NO. 3, June 1979. https://accelconf.web.cern.ch/p79/PDF/PAC1979_3209.PDF
21. Méot, F.: Polarized Beam Dynamics and Instrumentation in Particle Accelerators, USPAS Summer 2021 Spin Class Lectures, Springer Nature, Open Acess (2023). https://link.springer.com/book/10.1007/978-3-031-16715-7
22. Lee, S.Y: Spin Dynamics and Snakes in Synchrotrons. World Scientific (1997)
23. Aknin, J.P., et al.: Status report on rejuvenating SATURNE and future aspects. PAC 1979 Conference. IEEE Tans. Nucl. Sci., Vol. NS 26, No. 3, June 1979. https://accelconf.web.cern.ch/p79/PDF/PAC1979_3138.PDF
Figure 10.7: Copyrights under license CC-BY-3.0, https://creativecommons.org/licenses/by/3.0; no change to the material; “SPES IV” has been added on the picture
24. D. L. Rubin, et al.: Upgrade of the Cornell electron storage ring as a synchrotron light source. WEPOB36, Proceedings of NAPAC2016, Chicago, IL, USA. https://accelconf.web.cern.ch/napac2016/papers/wepob36.pdf